

UNIVERSITY OF CAMBRIDGE

FINAL YEAR PROJECT

Boundary Layer Ingesting Propulsion of Hybrid Airships

Fritz Kirchner

supervised by
Dr. Cesare Hall
Dr. Sam Grimshaw

May 31, 2017

Abstract

The theoretical principle of boundary layer ingestion (BLI) is that for a reduced inflow velocity, an aircraft's propulsor requires less power to achieve the same thrust as a propulsor located in higher-speed inlet flow. The benefits of BLI on fuel efficiency are due to the re-energisation of the low-speed aircraft wake, which reduces the wasted kinetic left behind the aircraft and increases the propulsive efficiency of the propulsor. Moreover, the entrainment of flow into the propulsor can delay the separation of the fuselage boundary layer leading to reductions in aircraft's drag.

Hybrid airships, a relatively new class of airship that combine the benefits of buoyant and aerodynamic lift, can capitalise on this increase in fuel efficiency due to the boundary layer ingesting propulsion system at the rear of the airship. This experimental project therefore sought to measure the effectiveness of a boundary layer ingesting propulsion system for a model hybrid airship in a closed-section wind-tunnel, with two 3D printed propulsors at a Reynolds number of 8×10^5 .

The objective of the project is to design an experiment that can capture the changes in fuel efficiency due to BLI for a range of propulsor positions downstream of the airship. The results can then be used to propose guidelines for the optimum location of the propulsors for a hybrid airship to maximise the BLI effect.

Additionally, a theoretical control volume analysis of the integrated airship and propulsor system was conducted in order to model the BLI effect. The preliminary integrated tests show that similar trends in the power saving coefficient, a proxy for fuel efficiency, between the experimental and theoretical results can be observed. The results indicate that the power saving coefficient could as high as 9.8% with a boundary layer ingesting propulsion system.

The propulsors and airship were also tested separately to assess the flow aerodynamics and performance compared with the design model. The experimental results for the propulsor showed that separation of stators was causing the propulsor to run at a 18% lower mean flow coefficient ($\bar{\phi} = 0.5$) than design. As such, it was shown that 2D design theory alone is inadequate to model the flow dynamics of a low Reynolds number and low hub-tip ratio compressor. Despite the lower mass flow rate, the propulsor was still able to achieve its design objective of producing sufficient thrust to balance the airship's drag.

The traverse results downstream of the airship were able to successfully resolve the airship's wake and vorticity flow fields. The experimental results also showed that the airship's flow field was very sensitive to the interaction between the fairing and the airship, which led to an asymmetric flow field in the horizontal plane.

There is plenty of scope for further work on this rig. A redesign of the fairing and pylon to reduce the asymmetry of the airship's flow; investigation into the effects of the inlet distortion on the propulsor's turbomachinery; and further development of the theoretical BLI model to incorporate the effects of distortion on the propulsor's performance.

Acknowledgements

The author wishes to acknowledge the support of Dr. C. Hall and Dr. S. Grimshaw, the supervisors for this project, for their invaluable advice throughout the project, and I. Thornton, a *Whittle Laboratory* technician, for generously devoting his time to building and setting up the rig.

Contents

1	Introduction	6
1.1	Background	6
1.2	Motivation	7
1.3	Project Aims	7
2	Theory	8
2.1	Power Saving Coefficient	8
2.2	Effect of the Inlet Velocity on Fuel Efficiency	8
2.3	Power Balance Approach	9
2.4	Modelling the Benefits of Boundary Layer Ingestion	11
3	Experimental Design	15
3.1	Wind-tunnel Design	15
3.2	Hybrid Airship Design	19
3.3	Propulsor Design	22
4	Results and Discussion	30
4.1	Aerodynamics of the Propulsor	30
4.2	Aerodynamics of the Hybrid Airship Assembly	39
4.3	Impact of Boundary Layer Ingestion on the Hybrid Airship's Performance .	42
4.4	Future Development	47
	Appendices	49
	A Steady-Flow Momentum Equation of a Propulsor	50
	B Thrust and Net Thrust Analysis	51
	C Radial Equilibrium Theory	52
	D Detailed Blade Design Parameters	54
	E Power Law Boundary Layer Profile	55
	F Transformation from Cartesian to Polar	56
	G Blade Design Theory	57
	H Traverse Control Volume Analysis	63
5	References	65

Nomenclature

Non-dimensional Blade Properties

ϕ	Flow coefficient
ψ	Stage loading
Λ	Reaction
DF	Diffusion factor
η_{is}	Isentropic propulsor efficiency

Blade Angles

α_1	Rotor absolute inlet angle
α_2	Stator absolutely inlet angle
β_1	Rotor relative inlet angle
β_2	Stator relative inlet angle
χ_1^r	Rotor inlet metal angle
χ_2^r	Rotor exit metal angle
χ_2^s	Stator inlet metal angle
χ_3^s	Stator exit metal angle
δ	Rotor deviation
γ	Stagger angle
θ	Camber angle
i_1	Rotor incidence
i_2	Stator incidence

Blade Geometry

c	Blade chord
l	Blade pitch
s	Blade span
t	Blade thickness
Z	Blade number

Other Symbols

Ω	Angular velocity
ω	Vorticity

U	Blade tangential velocity
V	Absolute velocity
W	Relative velocity
Δh_0	Stagnation enthalpy change
Δp_0	Stagnation pressure change
p_0	Stagnation pressure
p	Static pressure
NR	Nozzle ratio
AR	Aspect ratio
F	Thrust
P	Input power
\dot{m}	Mass flow rate
\dot{Q}	Volumetric flow rate
D, \varnothing	Diameter
L	Length
C_D	Drag coefficient
C_L	Lift coefficient
C_F	Thrust coefficient
C_{p0}	Stagnation pressure coefficient
C_p	Static pressure coefficient
n	Swirl distribution parameter
Ne	Newton number
Re	Reynolds number
M	Mach number
S	Area
δ^*	Displacement thickness
θ	Momentum thickness
H	Shape factor
\dot{E}_a	Axial kinetic energy deposition rate
Φ_s	Surface dissipation rate
Φ_w	Wake dissipation rate
ρ, ν	Density, kinematic viscosity

P_K Mechanical power

$()_r$ Rotor blade

Subscripts

$()_{ext}$ External propulsor flow

$()_s$ Stator blade

$()_h$ Hub

$()_x$ Axial

$()_m$ Mid-span

$()_\theta$ Tangential

$()_c$ Casing

$()_a$ Internal flow of the propulsor

$(\bar{})$ Mass-averaged mean

$(\bar{})_1$ Flow into the control volume

$(\bar{})_\infty$ Freestream

$(\bar{})_2$ Flow out of the control volume

$(\bar{})_w$ Aircraft wake

$(\bar{})_i$ Section i of the propulsor

$(\bar{})_j$ Propulsor jet

$(\bar{})_{ij}$ Grid value i,j

$(\bar{})_{BLI}$ Boundary layer ingestion

$(\bar{})_{LE}$ Leading edge

$(\bar{})_{non-BLI}$ No boundary layer ingestion

$(\bar{})_{TE}$ Trailing edge

1 Introduction

1.1 Background

A boundary layer ingesting propulsion system can improve the fuel efficiency of an aircraft by placing the propulsor in a region of low speed flow (i.e. the wake of an aircraft). The potential improvements in fuel efficiency for the aircraft as a result of boundary layer ingestion (BLI) are due to the re-energisation of the low-speed aircraft wake [1], which increases the propulsive efficiency of the propulsor, and the delayed separation of the fuselage boundary layer due to entrainment of flow into the propulsor, which reduces the aircraft's drag [2].

The benefits to the propulsive efficiency from re-energizing the aircraft wake were demonstrated by Plas et al. for an idealised propulsor shown in Fig. 1 [1]. They showed that for a constant mass flow rate, the power required for a given thrust was higher for a podded than a boundary layer ingesting propulsor: $P_{non-BLI} > P_{BLI}$.

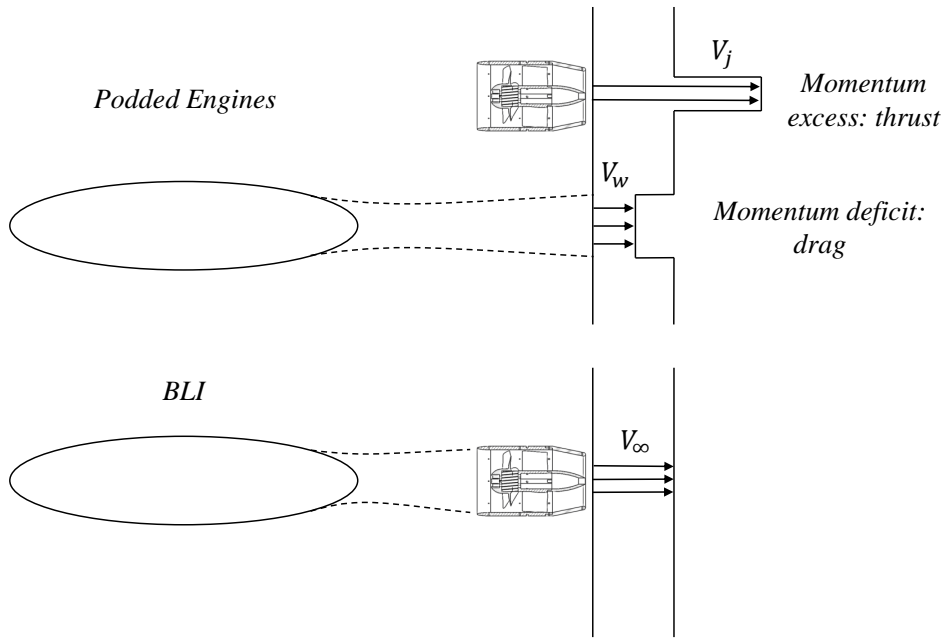


Figure 1: Benefits of BLI-podded case and 100% BLI. The momentum excess created by the propulsor balances the momentum deficit created by the airframe

The idealised propulsor considered in Fig. 2, however, does not account for the effects of inlet distortion on the aerodynamics of the turbomachinery. Plas et al. showed that the effects of stagnation pressure non-uniformity upstream of a fan has a major impact in determining the impact of BLI on overall fuel burn [1]. As such, while a propulsor located in the free-stream versus a propulsor located in the wake of a fuselage should, in theory, require less power to produce the same thrust, the benefits may not always be realisable in practice.

1.2 Motivation

The hybrid airship is a variant of the conventional, one-lobe airship, which combines the benefits of both buoyant and aerodynamic lift. The buoyant lift of the airship is provided by the inert helium within the airship, while the aerodynamic lift is due to the airship's aerodynamic multi-lobe design that can generate over 3 times the aerodynamic lift of the conventional airship [3]. A common drawback of conventional airships is the need for a mast or routine tie-downs. However, the hybrid can modulate its aerodynamic lift at take-off and landing to eliminate this need. The improvements to the operational flexibility and robustness as a result of the increased aerodynamic lift gives the hybrid airship a competitive edge over the conventional airship design.

The British airship manufacturer, *Hybrid Air Vehicles Limited*, is developing the *Airlander 10*, a hybrid airship with a total of four three-bladed ducted propellers: two of the propellers are positioned alongside the side of the fuselage and the other two are located towards the rear of the airship [4]. The two rear propulsors located in the boundary layer wake have the potential to improve the fuel efficiency of the aircraft through the effects of BLI. Their position at the rear of the aircraft means that they will be able to ingest the wake generated on the upper and lower surfaces of the aircraft hull.

Along with the non-axisymmetric shape of the hybrid airship, there are several practical design drivers that may dictate a non-axial position for the propulsors. These may include: interactions between multiple propulsors, constraints on position, flow distortion effects on propulsor efficiency [1] and interaction with the fins. Computational simulations of the *Airlander 50* have visualised the complicated interactions between vortices that form on the airship due to the ellipsoidal shape of the body and fins [5]. It is not yet fully understood, however, what the overall effect of these interactions will have on the effectiveness of BLI for different positions of the propulsors for a hybrid airship.

1.3 Project Aims

The primary objectives of this project are to:

1. Establish an experiment to explore the effectiveness of boundary layer ingestion for hybrid airships.
2. Design and test a scaled propulsor that provides sufficient thrust for the experiments.
3. Investigate the flow field downstream of an airship with and without BLI.
4. Propose guidelines for locating propulsors relative to an airship given the competing and complex interactions of the flow.

2 Theory

2.1 Power Saving Coefficient

The objective of this project is to measure the changes in the input power of a boundary layer ingesting propulsion system as a function of the propulsors' positions behind the hybrid airship. For a constant motor efficiency, the input motor power to the propulsor is then directly related to the aircraft's fuel burn. Conventional figures of merit for the efficiency of a propulsor are propulsive efficiency and specific fuel consumption, but as described in Appendix B, the net thrust decreases with BLI. Therefore, a decrease in either variable may not necessarily indicate an increase in the fuel efficiency as the net thrust is not constant. Instead, Plas et al. [1] recommended using the power saving coefficient (PSC) to evaluate the effectiveness of BLI, which will be used as the figure of merit in Section 4.3. The PSC is defined as:

$$PSC = \frac{P_{non-BLI} - P_{BLI}}{P_{non-BLI}} \quad (1)$$

where $P_{non-BLI}$ is the input power to a propulsor located in the free-stream, while P_{BLI} is the input power to an identical propulsor located in the aircraft wake for the same net force on the overall aircraft. The use of PSC is then directly related to the electrical power efficiency.

2.2 Effect of the Inlet Velocity on Fuel Efficiency

Plas et al. [1] considered the idealised propulsor in Fig. 1 to demonstrate the effects of inlet velocity on fuel efficiency for a constant mass flow rate and thrust. Similarly, for the control volume shown in Fig. 2 the effect can be demonstrated with the constant mass flow rate assumption relaxed.

By applying the steady-flow momentum equation (SFME) and steady-flow energy equations (SFEE) to the control volume (Appendix A), it can be shown that for a given thrust, the change in velocity from inlet to outlet of the control volume is a function of the inlet velocity, such that:

$$F = \dot{m}_a \Delta V \quad (2)$$

$$\Delta V = -\frac{V_1}{2} \pm \frac{\sqrt{V_1^2 + 4k^2}}{2} \quad (3)$$

where $k^2 = \frac{F}{\rho A_2}$.

At subsonic conditions, the change in power of the propulsor with respect to the inlet velocity for a given thrust and nozzle area is therefore a function of the inlet velocity only.

As such, it can be shown that for a higher inlet velocity, the power required for a given thrust will increase for all $V_1 \geq 0$.

$$P = F \left(V_1 + \frac{\Delta V}{2} \right) \quad (4)$$

$$\frac{\partial P}{\partial V_1} = F \left(\frac{3}{4} \pm \frac{V_1}{4\sqrt{V_1^2 + 4k^2}} \right) > 0 \quad \forall V_1 \geq 0 \quad (5)$$

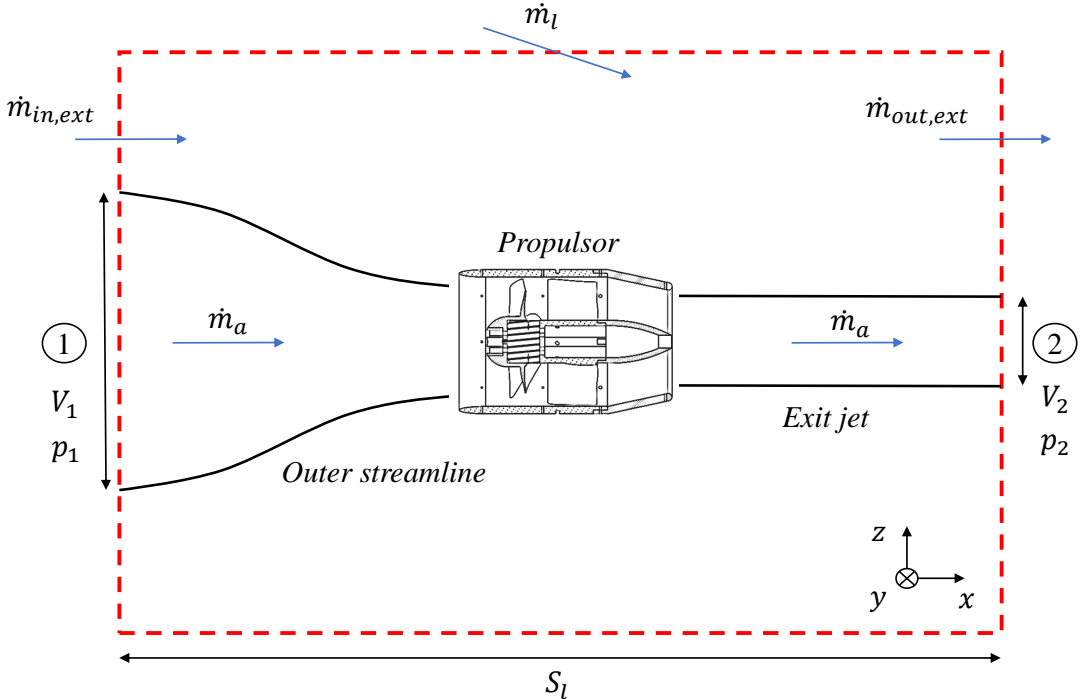


Figure 2: Control volume to find the power as a function of the inlet velocity for a constant propulsive force

2.3 Power Balance Approach

The tightly-integrated nature of propulsion and boundary layer control systems makes it challenging to separate the thrust and drag components to perform an accurate momentum-equation analysis. As such, Drela [6] formulated the framework to conduct a control volume analysis that focuses on mechanical power and kinetic energy flow. The method does not require any separate definitions of thrust and drag, and hence is particularly useful in the boundary layer ingestion analysis.

The power balance approach will be applied to the control volume analysis of the traverse results in Section 4.3, where it will be used to estimate the power dissipation of the airship and assembly for the integrated and non-BLI configurations.

The integral power balance equation is given by:

$$P_S + P_V + P_K = Wh + \dot{E}_a + \dot{E}_v + \dot{E}_p + \dot{E}_w + \Phi \quad (6)$$

where:

P_S	Net propulsor shaft power	\dot{E}_v	Wake transverse kinetic energy deposition rate
P_V	Net pressure-volume power	\dot{E}_p	Wake pressure-defect work rate
P_K	Mechanical power into CV	\dot{E}_w	Lateral wave-outflow energy deposition rate
Wh	Potential energy rate	\dot{E}_a	Wake streamwise kinetic energy deposition rate
Φ	Viscous dissipation rate		

For the simple 2D case shown in Fig. 1, it is assumed that the aircraft is propelled by an isolated ideal propulsor.

Therefore, Eq. 6 can be simplified to give:

$$P_K = \dot{E}_a + \Phi \quad (7)$$

The rate of streamwise kinetic energy being deposited in the flow out of the CV is defined as:

$$\dot{E}_a = \int_{S_{TP}} \frac{1}{2} \rho (V_{TP} - V_\infty)^2 V_{TP} dS$$

where V_{TP} is the velocity of the flow at the Trefftz-plane. Note that this is always positive, both in the case of a propulsive jet and a wake.

The total dissipation, Φ in the flowfield is equal to the dissipation due to the aircraft's surface, Φ_s and the dissipation in the trailing wake, Φ_w . This gives that the power from the motor is equal to the streamwise kinetic energy out of the control volume plus the total energy dissipated in the boundary layer and trailing wake.

$$P_K = \dot{E}_a + \Phi_s + \Phi_w \quad (8)$$

Downstream of the trailing edge of the wake and the propulsor exit, the streamwise kinetic energy is gradually dissipated. If the exit Trefftz plane is chosen to be sufficiently far downstream, the streamwise kinetic energy from the propulsor jet effectively disappears and is equal to the total wake dissipation such that:

$$\Phi_s + (\dot{E}_a)_{TE} = \Phi_{total} = \Phi_s + (\Phi_w)_{TP} \quad (9)$$

$$\therefore \dot{E}_a(x) + \Phi_w(x) = \Phi_{total} - \Phi_s \quad (10)$$

where x is the axial distance downstream of the aircraft trailing edge.

For the ideal BLI case, the propulsor generates a filled-in wake with $V_{TP} = V_\infty$. In this case $\dot{E}_a = 0$ and the net propulsor mechanical power is given by:

$$P_{BLI} = \Phi_s \quad (11)$$

For the non-BLI case, the net propulsor mechanical power is given by:

$$P_{non-BLI} = \Phi_{total} \quad (12)$$

Hence, the difference in power between the BLI and non-BLI case is due to the downstream dissipation of streamwise kinetic energy in the wake:

$$\Delta P = \Phi_w = \dot{E}_a(x) \quad (13)$$

By ingesting the wake, we eliminate any subsequent dissipation of the wake, which is equal to the wake streamwise kinetic energy dissipation rate, \dot{E}_a , at the point of ingestion. As such, we expect the maximum power savings from BLI to be achieved at the point of maximum \dot{E}_a , which is generally at the trailing edge of the aircraft. Therefore, the benefit from BLI decreases the further away the propulsors are located downstream of the point of the trailing edge.

2.4 Modelling the Benefits of Boundary Layer Ingestion

One of the benefits of boundary layer ingestion is ingesting and re-energising the aircraft wake. This section of the report presents a model for assessing the change in effect on the PSC of an idealised propulsor and aircraft as a function of a propulsor's position relative to the aircraft. The results of the model will be used to predict how the PSC changes with the boundary layer shape factor and the propulsor's position for an idealised power-law boundary layer profile (Appendix E). Moreover, the results obtained from the traverse experiments of the airship's flow field can be used as inputs into the model to estimate the change in PSC for an idealised propulsor.

The net drag of the aircraft consists of three components: the aircraft drag, propulsor drag and ingested drag.

$$D_{net} = D + D_{nacelle} - D_{ingested} \quad (14)$$

where D is the drag due to aircraft body's boundary layer and wake.

Assuming that the nacelle drag is negligible, the net drag is given by:

$$D_{net} \approx D - D_{ingested} \quad (15)$$

By applying mass conservation to the control volume given in Fig. 3 and assuming a uniform jet velocity at the nozzle exit, the propulsor's jet velocity is given by:

$$V_j = \frac{1}{S_2} \int_{S_1} V_w(x, y) dS \quad (16)$$

where S_2 and S_1 are the nozzle exit and inlet streamtube areas of the propulsor respectively.

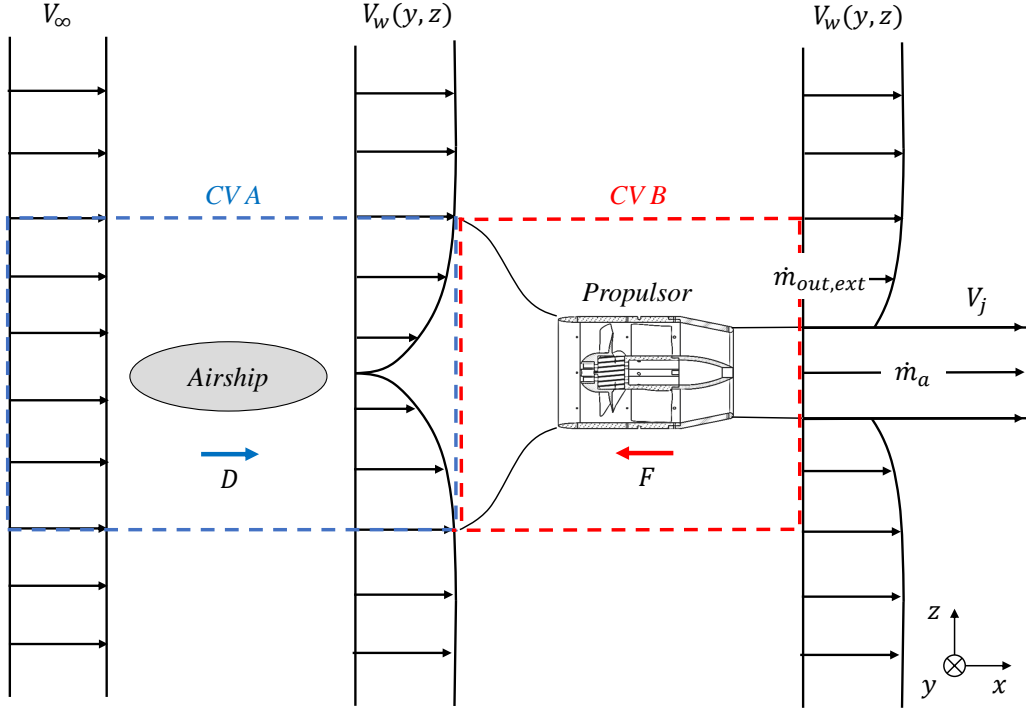


Figure 3: Hybrid Airship and Propulsor Control Volumes (not to scale)

For an aircraft at cruise, the net thrust is equal to the net drag of the aircraft. By applying the SFME in the x direction, it can be shown that the ingestion of the aircraft wake does not reduce the required propulsor thrust. As such, for both the BLI and non-BLI cases, the drag is equal to the thrust.

$$D = \int_{S_2} V_j d\dot{m} - \int_{S_1} V_w(y, z) d\dot{m} \quad (17)$$

Combining the results from Eq. 16 and 17, we can derive a non-linear equation as a function of the inlet streamtube area.

$$D = \rho V_j^2 S_2 - \int_{S_1} \rho V_w^2(y, z) dS \quad (18)$$

$$f(S_1) = \frac{D}{\rho} - S_2 \left(\int_{S_1} V_w(y, z) dS \right)^2 + \int_{S_1} V_w^2(y, z) dS = 0 \quad (19)$$

Assuming that the surface S_1 is approximately axisymmetric, the non-linear equation can be solved using a bisection method to determine the size of S_1 , and hence the jet

velocity, V_j .

Applying the SFEE to the control volume B, the power required by the motor can be determined. It is assumed that the flow is adiabatic, $\dot{Q} \approx 0$, and that the control volume is sufficiently far upstream and downstream of the propulsor so that the inlet and exit temperatures are approximately equal, $\Delta T \approx 0$.

$$\dot{Q} - W_x = \oint_{CS} h_0 d\dot{m} \quad (20)$$

$$-W_x \approx \frac{1}{2} \oint_{CS} V_w^2 d\dot{m} \quad (21)$$

$$P_K = -W_x = \frac{1}{2} \rho V_j^3 S_2 - \frac{1}{2} \rho \int_{S_1} V_w(y, z)^3 dS \quad (22)$$

The results from the theoretical model for an idealised power law boundary layer (see Appendix E) are shown in Fig. 4. The shape factor, which is an indicator of the likelihood of separation (laminar: $H \approx 3.5$ and turbulent: $H = 2.4$ [7]), was calculated for a range of boundary layer profiles. As the shape factor increases, the momentum deficit within the boundary layer increases. The model therefore predicts that for a higher shape factor, the PSC increases. The physical mechanism behind this trend, which was also found by Smith [8], is that for a higher shape factor, the average velocity of the ingested drag is lower.

The theoretical model also predicts that the PSC decreases as the propulsor moves vertically away from the centre-line of the boundary layer. Physically, as the propulsor moves away from the boundary layer, the propulsor ingests less of the boundary layer drag. Hence a lower volume of low-momentum fluid is re-energised by the propulsor.

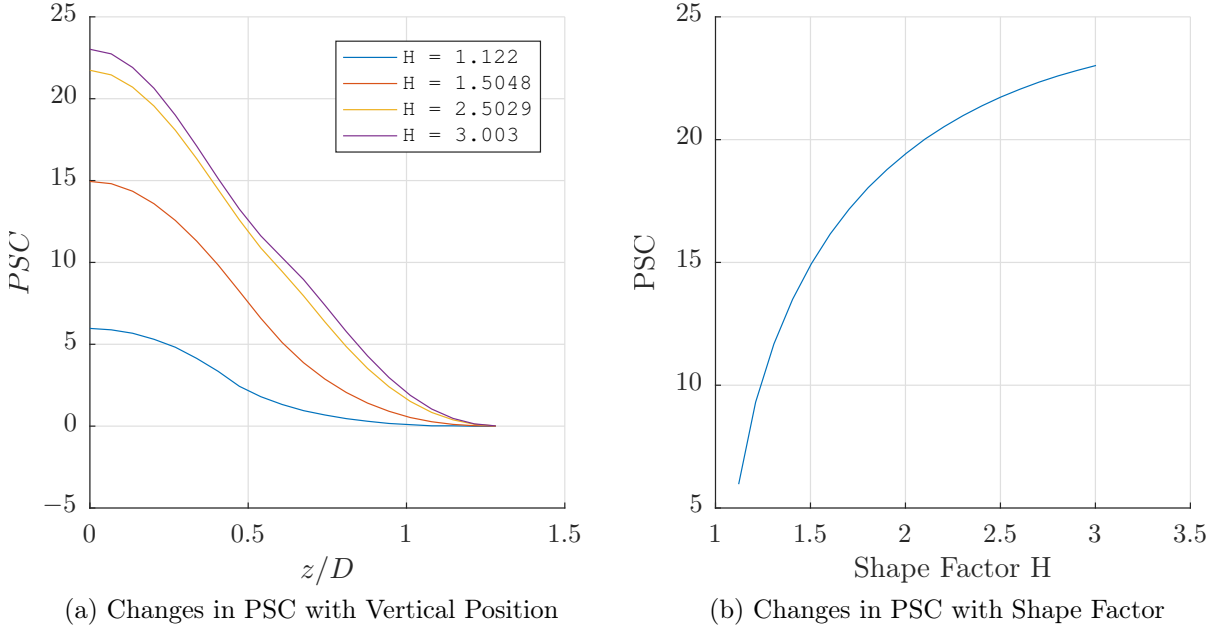


Figure 4: BLI theoretical model results for PSC variation with shape factor and vertical propulsor position

The idealised BLI model does not account for changes in the propulsive efficiency as a result of inlet distortion on the turbomachinery. Moreover, it assumes that the propulsor is located sufficiently downstream of the airship such that the flow field behind the aircraft is unaffected by the presence of the propulsor. While this is a crude assumption given the coupled nature of the thrust and drag in an integrated propulsion system, the theoretical results should still highlight the trends we expect to see from the experimental results in Section 4.3.

3 Experimental Design

3.1 Wind-tunnel Design

Sizing the wind-tunnel

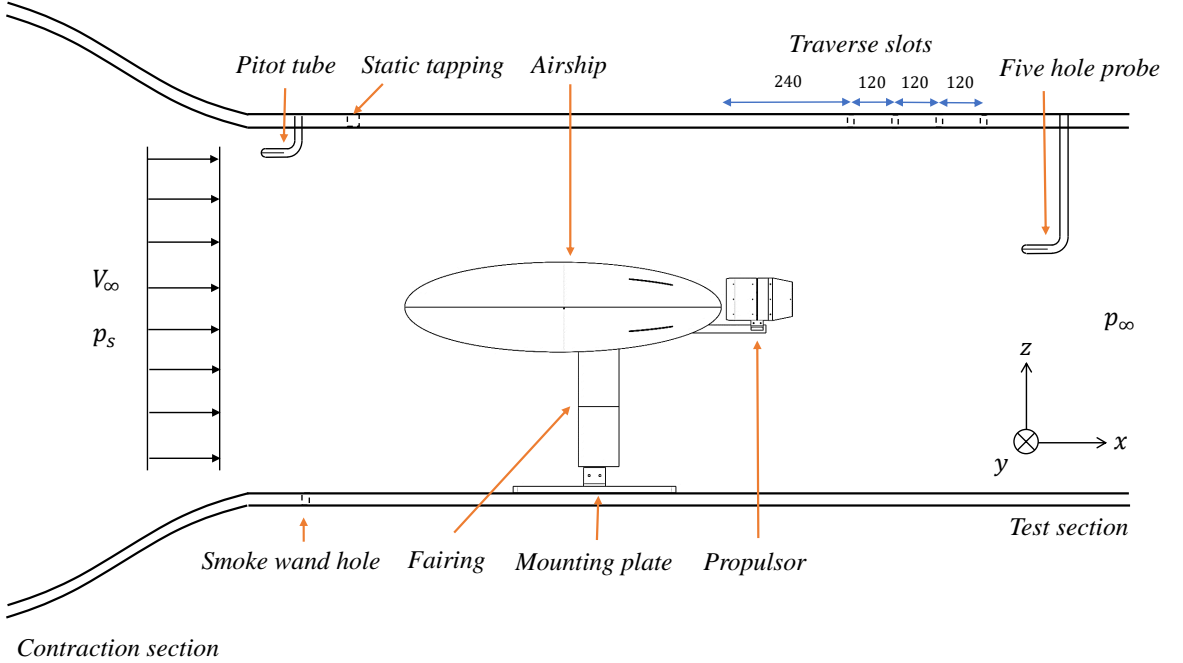


Figure 5: Wind-tunnel set-up cross-section (units in mm)

The effectiveness of the boundary layer ingestion was determined experimentally by testing a hybrid airship in a wind-tunnel at the *Whittle Laboratory*. The expected wind-tunnel flow-rate was measured using a pitot-static tube to be $\dot{Q} = 9.9 m^3/s$. For a fixed volume flow rate, the velocity through the wind-tunnel is inversely proportionally to the width of the tunnel squared. For a fixed blockage ratio (i.e. cross-sectional airship to wind-tunnel area), the length of the airship scales proportionally with the wind-tunnel's width. The Reynolds number for the airship therefore scales inversely proportionally with the wind-tunnel's width.

$$Re = \frac{vL}{\nu} \sim \frac{1}{D} \quad (23)$$

In order to maximise the scale model Reynolds number to more closely match that of the *Airlander 10*, the wind-tunnel width was minimised, while subject to the constraint of maximising the ratio of the airship to propulsor size. A characteristic size ratio for the airship to propulsor is defined as:

$$\text{Propulsor Size Ratio} = \frac{Vol^{2/3}}{D^2} \quad (24)$$

Given the high Reynolds number of hybrid airships and the minimum size of the

propulsor required to meet the thrust requirements for the experiment, neither the Reynolds number nor the proportion of the model propulsor to airship size ratio could be matched using the equipment available (Table 1). Nonetheless, while the absolute values obtained from the experiment may not be representative of the real airship, it is expected that the trends obtained from the experiments will still be useful as a preliminary assessment of the boundary layer ingesting effect.

Parameter	Airlander 10	Model	Units
Length	90	0.584	m
Height	43.5	0.165	m
Width	26	0.305	m
Speed	41.1	20	m/s
Volume	38000	0.0169	m ³
Re	2.6×10^8	7.7×10^5	
Airship to Prop. Ratio	502	22	

Table 1: Hybrid Airship Dimensions

Parameter	Value	Units
Height	0.66	m
Width	0.75	m
Cross-sectional Area	0.495	m ²

Table 2: Wind-tunnel Dimensions

Pylon and Fairing Design

Initial traverse testing of the airship and rectangular strut showed significant interference between the flow around the airship and the wake forming behind the strut. In order to improve the aerodynamics of the structure, a fairing was designed and 3D printed in the *Dyson Laboratory*.

A NACA 0020 airfoil [9] was used for the design. The co-ordinates for the airfoil were derived from Eq. 25.

$$y = 5t \left(0.2969 \sqrt{\frac{x}{c}} - 0.1260 \left(\frac{x}{c} \right) - 0.3516 \left(\frac{x}{c} \right)^2 + 0.2843 \left(\frac{x}{c} \right)^3 - 0.1036 \left(\frac{x}{c} \right)^4 \right) \quad (25)$$

where t = maximum thickness as a fraction of the chord.

Eq. 25 was solved for a range of thickness and chord lengths subject to the boundary conditions given in equations 26 - 28, which ensure that the airfoil both encompasses the rectangular strut and has zero camber.

$$y = W/2, x = x_0 \quad (26)$$

$$y = W/2, x = x_0 + L \quad (27)$$

$$y = y_{max}, x = 0.3c \quad (28)$$

where W = width of the strut and L = length of the strut.

The final airfoil thickness and chord-length were then selected to minimise the airfoil area. *XFOIL*[21], a viscous 2D solver, was used to carry out a simulation of the airfoil at $Re = 1 \times 10^5$ and $M = 0.058$ to ensure that the flow around the fairing did not separate. The results of the 2D simulation (Fig. 6) show that a laminar bubble forms on the surface of the airfoil and then reattaches. The flow is therefore attached at the trailing edge and the fairing wake is kept small.

Parameter	Value	Units
t	20	%
c	78	mm
Re	1×10^5	

Table 3: Airfoil Design

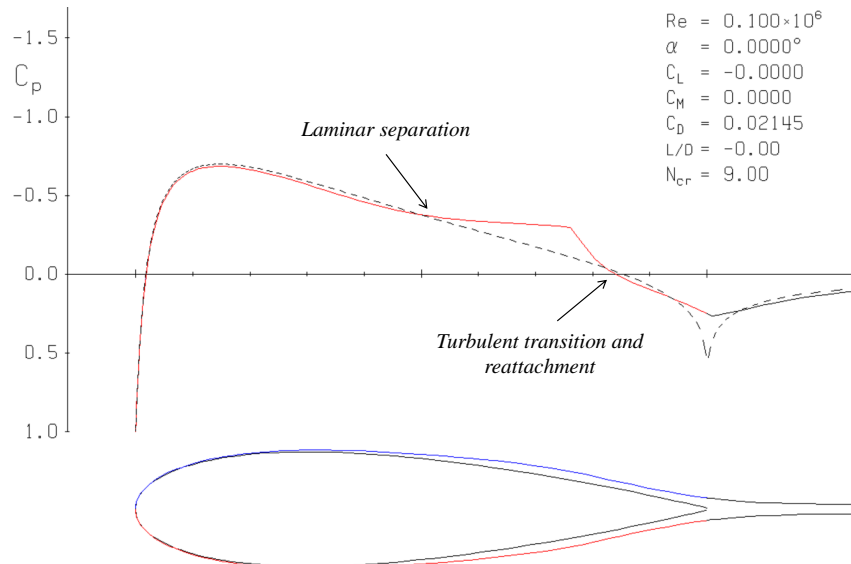


Figure 6: *XFOIL* Analysis Results

Instrumentation

The wind-tunnel set-up used for the experiments is shown in Fig. 7. The experiment was designed almost entirely from scratch by the author, although in the interest of time the 5-hole probe calibration and *Labview* script were obtained from Dr. Grimshaw.

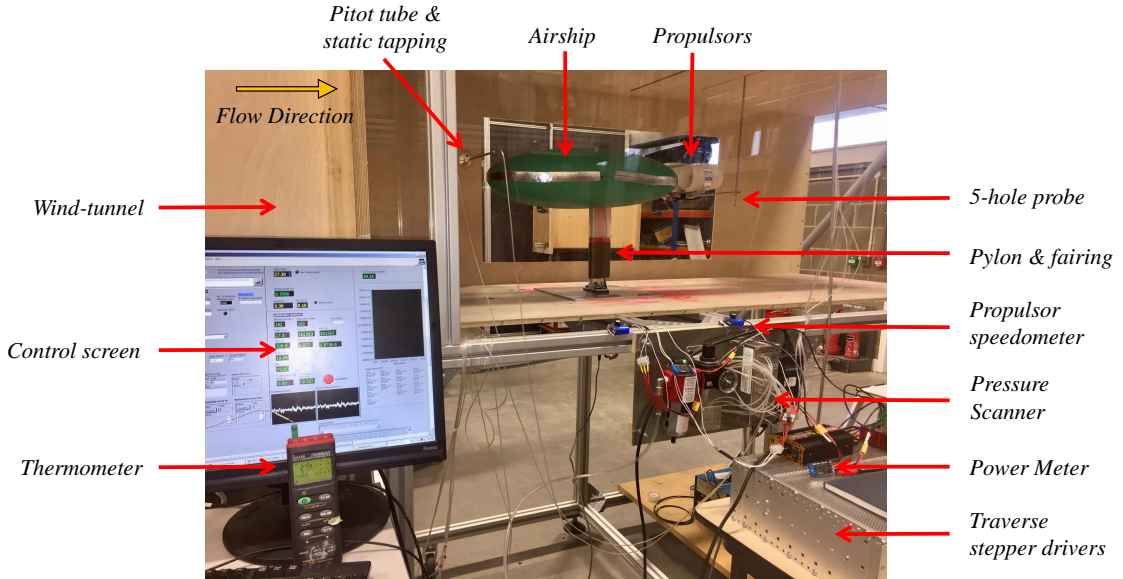


Figure 7: Photograph of experimental set-up

The thrust and drag of the propulsors and airship respectively were measured using a load cell. The airship was mounted directly on the load cell so that the drag force on the fairing was isolated from the load cell measurement. The voltage from the load cell was recorded with an analog-to-digital data acquisition card, and converted into a force using the linear calibration data obtained prior to each traverse.

The five-hole probe and traverse equipment were used to analyse the pressure and velocity flow fields downstream of the propulsor and airship. The probe head has a diameter of 2 mm (2.6% of the propulsor diameter) with faceted faces at 45°. It is calibrated using a *Whittle Laboratory* calibration tunnel. The calibration was performed for ±30° in yaw angle and ±20° in pitch at 2° intervals. The internal geometry of the probe and connecting tubes is designed to give a fast settling time. In both calibration and experimental measurements the probe settling time is 0.5s, and after this, the pressure recording is averaged for 1 second.

The two speed controllers for the propulsors were located outside the wind-tunnel and were set to give a fixed power output before running each traverse. The drift in the power over an hour-long traverse was observed to be approximately 1 – 2W (2 %). This was manually recorded at the start and end of the experiment and the average was used in all calculations.

3.2 Hybrid Airship Design

Geometric Parametrisation of the Hybrid Airship

Parameter	Value	Units
Volume	0.0169	m^3
Cross-sectional Area	0.0423	m^2
Surface Area	0.407	m^2

Table 4: Hybrid Airship Dimensions

The blockage ratio is defined as the maximum cross-sectional area of the airship divided by the cross-sectional area of the wind-tunnel section. Barlow [10] recommends the blockage ratio should be between 5 – 10%. The hybrid airship was scaled according to the dimensions of the *Hybrid Air Vehicles Airlander 10* [4] such that the blockage ratio was within the recommended blockage ratio range.

$$\text{Blockage Ratio} = 8.5\% \quad (29)$$

The hybrid airship design is an approximate 158:1 scale model of the *Hybrid Air Vehicles Airlander 10* (Fig. 8). The hybrid airship consists of three parallel ellipsoids: inner ellipsoid of $\varnothing = 145mm$ and two outer ellipsoids of $\varnothing = 165mm$. The outer two ellipsoids are swept to follow a curved spline from the midpoint so that the tips intersect at the front end of the airship.

The model is machined from polyurethane tooling board to give two 5 mm shells, which connect along the horizontal centre-line. The lower half connects the airship to the rear propulsors via a clamped rod that extrudes from the rear, while the upper half connects the airship to the load cell via an aluminium block (Fig. 9). The load cell connection has been designed so that future projects may vary the airship's angle of attack. The load-cell position was located at the centre-of-mass for the complete assembly to minimise any torque effects on the load-cell force measurements.

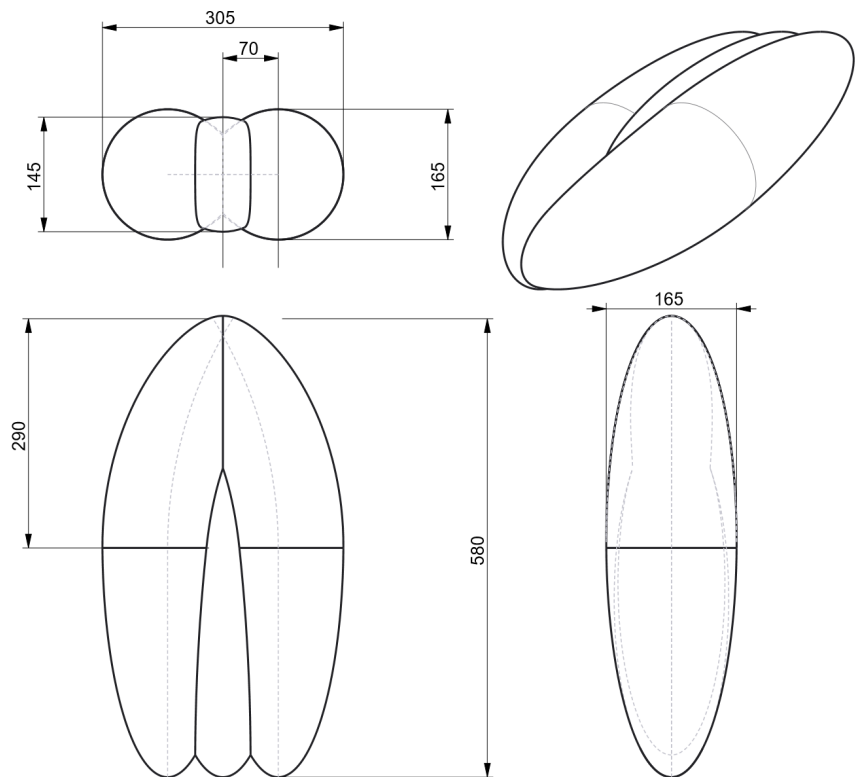


Figure 8: Hybrid Airship Design (Dimensions in *mm*)

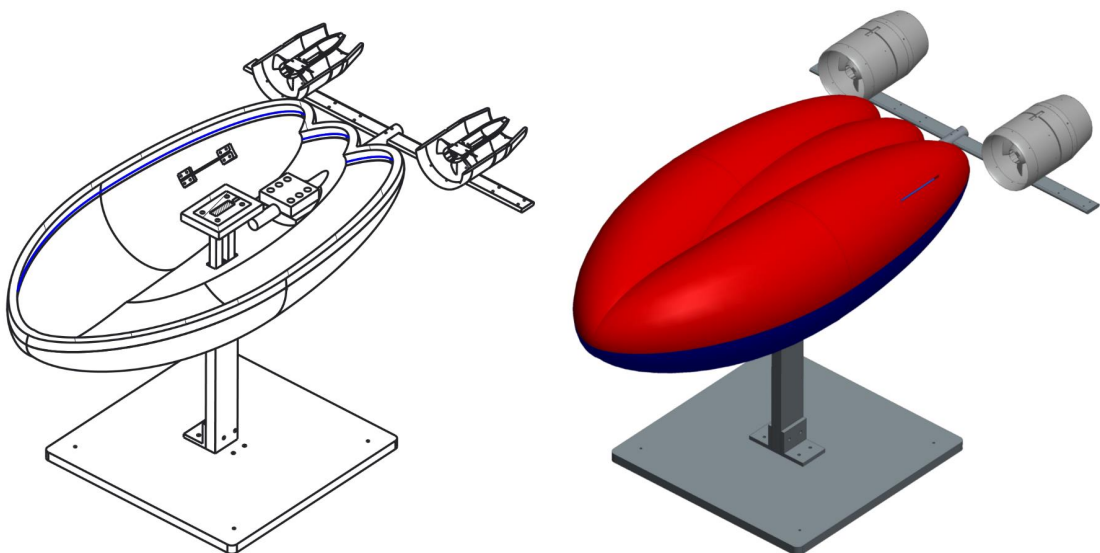


Figure 9: Hybrid Airship Assembly

Drag Estimation

The function describing the drag polar for a hybrid airship can be taken from a polynomial curve-fit of the appropriate set of data.

$$C_D = C_{D0} + kC_L^2 \quad (30)$$

where the drag coefficient for a hybrid airship is defined as:

$$C_D = \frac{D}{\frac{1}{2}\rho V_\infty^2 S} \quad (31)$$

$$S = Vol^{2/3} \quad (32)$$

For conventional and hybrid airships, the zero-lift drag coefficient can be estimated using Hoerner's drag equation [11] for streamline bodies.

$$C_{D0} = C_F \left(4 \left(\frac{l}{d} \right)^{1/3} + 6 \left(\frac{d}{l} \right)^{1.2} + 24 \left(\frac{d}{l} \right)^{2.7} \right) \quad (33)$$

where C_F is the friction coefficient, l is a characteristic length, and d is a characteristic diameter.

In Eq. 33 the first term on the right-hand side corresponds to the friction drag; the second term is the pressure drag; and the third is the drag due to separation. The friction coefficient C_F , can be estimated using Schoenerr's [11] formula (Eq. 34).

$$C_F = \frac{1}{(3.46 \log_{10} Re - 5.6)^2} \quad (34)$$

In practice, the hybrid airship will operate at its maximum lift-to-drag ratio, which is at an angle of attack of $\alpha = 10^\circ$ [5] and lift coefficient $C_L \approx 0.3$. Using the data available for the *Hybrid Air Vehicles Skycat 20*, a proxy drag coefficient polar can be determined for the hybrid airship [24]:

$$C_D = 0.043 + 0.67C_L^2 \quad (35)$$

Due to the limited time, the airship was only tested at a 0° angle of attack. However, the propulsors were originally designed to balance the drag of the airship when at its cruise angle of attack of 10° .

Parameter	Value	Units
C_D	0.11	
<i>D</i> rag	1.74	N

Table 5: Airship Drag at $C_L = 0.3$

The drag of the rear assembly was estimated using a conservative drag coefficient, $C_D = 0.47$, to give an assembly drag of $D_{assembly} \approx 1\text{ N}$. The total drag of the combined assembly for the purpose of designing the propulsor was estimated to be:

$$D_{total} = 2.74N \quad (36)$$

3.3 Propulsor Design

Propulsor Design Objectives and Constraints

Two single-stage compressors were designed, 3D printed and attached to the rear of the airship to simulate the thrust producing propulsors of a hybrid airship. To model the relative scales of the *Airlander 10*'s airship and propulsors as accurately as possible, the objective of the propulsor design was to minimise the outer diameter of the casing. Simultaneously, the propulsors were also subject to the following three constraints:

1. The minimum hub radius must be greater than the motor's radius. $r_h \geq r_{motor}$
2. The propulsors' thrust must exceed the total drag of airship and rear assembly. $F \geq \frac{D_{total}}{2}$
3. The input power must be less than the rated power of the motor. $P \leq P_{rated}$

The design constraints on the propulsor design are given in Table 6. The final motor selected for the propulsor was the *RC Quanum BE1806-2300kv Race Edition Brushless Motor*.

Parameter	Value	Units
r_{motor}	11.6	mm
F_{min}	1.37	N
P_{rated}	228.5	W

Table 6: Propulsor design constraints

The propulsor assembly was split into four sections: the stator casing, rotor casing, rear cone and nozzle. The stator blades were designed to reduce the swirl of the outlet flow, as well as provide the structural beams connecting the hub to the casing. The rotor casing, which rigidly attaches to the motor, consists of the rotor blades and houses the rotating shaft of the motor. The rotor casing design incorporates an inlet cooling system, which allowed air to flow through and over the motor to convect some of the heat being dissipated. Despite the inevitably detrimental effects this would have on the propulsor's aerodynamics, testing of an initial design showed that the high motor temperatures caused the rotor hub to weaken and melt (after 5 minutes of running at 60 W , temperatures in excess of 100°C were measured). Long-term operation at this temperature damaged the

motors' bearings, which caused the rotor blades to collide with the casing leading to critical blade failure.

The nozzle and inner cone at the rear, which accelerate the flow and sets the operating point of the propulsor, were designed to be easily detachable so that the motor and cables could be accessed during assembly. Pressure tappings were located at each section so that the inlet stagnation and static pressure at each section could be measured during testing. The stator blades were also designed with holes so that the motors' wires could be connected to the power without interfering with the internal propulsor flow. The inlet was designed using trial and error to eliminate inlet separation, which occurred during testing of an initial design (Fig. 11 (a)).

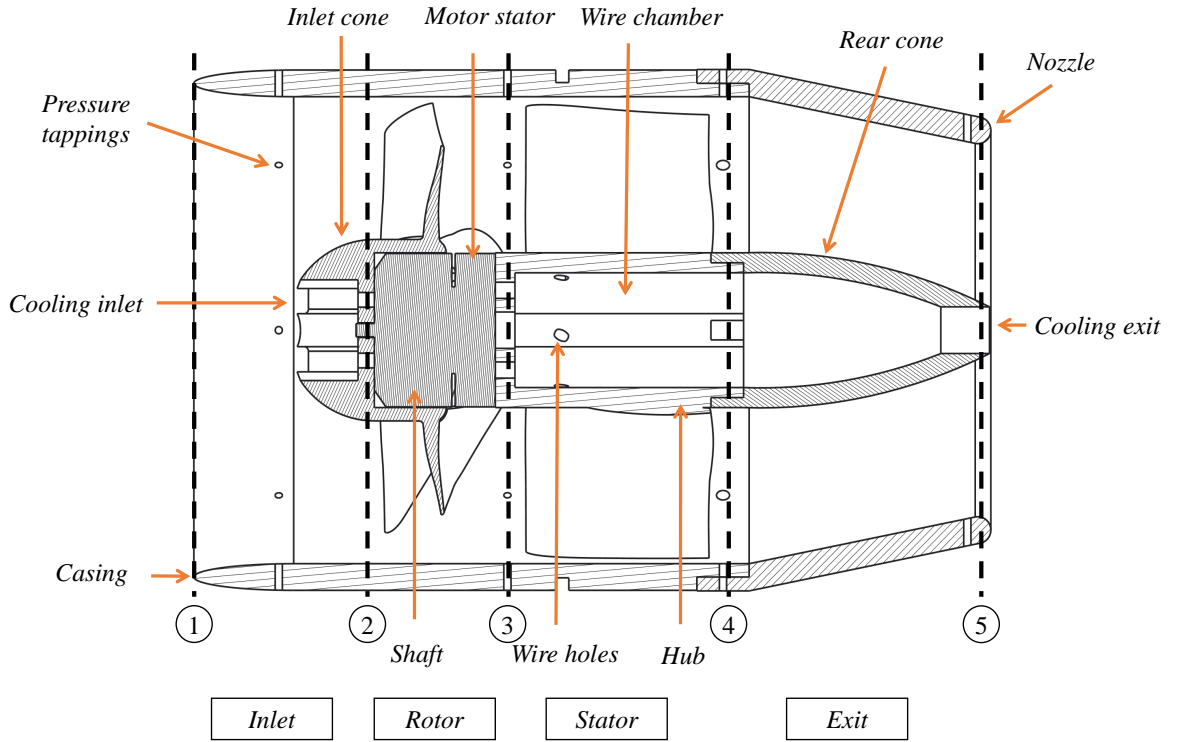


Figure 10: Propulsor Sections

Step 1: Sizing Propulsor and Radial Distributions

The initial step of the propulsor design was to calculate the minimum required casing radius for the propulsor, which was obtained by using the minimisation algorithm shown in Fig. 13. For an initial casing radius, the algorithm determines the force and power of the propulsor. If the force is below the minimum force required, the casing radius is incremented and the algorithm is looped until the minimum casing radius has been found, which satisfies both the force and power constraints.

Parameter	Value	Units	Parameter	Value	Units
Ω_{max}	18,000	rpm	ψ_m	0.35	
r_h	11.6	mm	n	0.1	
V_∞	20	m/s	η_{motor}	90	%
ϕ_m	0.6		η_{is}	50	%

Table 7: Inputs to the casing radius minimisation algorithm

For the inputs shown in Table 7 the minimal casing radius can be obtained. The maximum rotation rate is set by the motor’s flow factor Kv , which is the number of revolutions per minute that the motor will turn when 1V is applied with no load attached to the motor. The loading on the blades will reduce the maximum obtainable rotation rate, and as such the propulsor was designed to rotate at 50% of the maximum rotation rate with no loading.

Typical values for the flow coefficient and stage loading in a axial machine are $\phi = 0.4 - 0.8$ and $\psi = 0.3 - 0.4$ respectively [23]. For a fixed geometry and rotational speed, changes in the flow coefficient are proportional to changes in the mass flow rate through the machine. A high flow coefficient therefore implies a high mass flow rate and propulsor thrust. Maffioli [12] also showed that for low Reynolds numbers, flow coefficients as high as $\phi = 0.8$ are desirable for high rotor efficiency, while the allowable stage loading coefficients are dependent on the flow coefficient and at most reach $\psi = 0.5$.

Testing of an initial design with $\psi = 0.4$ exhibited full-span separation (Fig. 11). As such, a more conservative value of $\psi = 0.35$ was selected for the final design to reduce the likelihood of separation. Due to the low hub-tip ratio of the propulsor, engineering judgement was used in selecting the flow coefficient to ensure the shape of the blades was reasonable near the hub. A flow coefficient of $\phi = 0.6$ was selected for the final design.

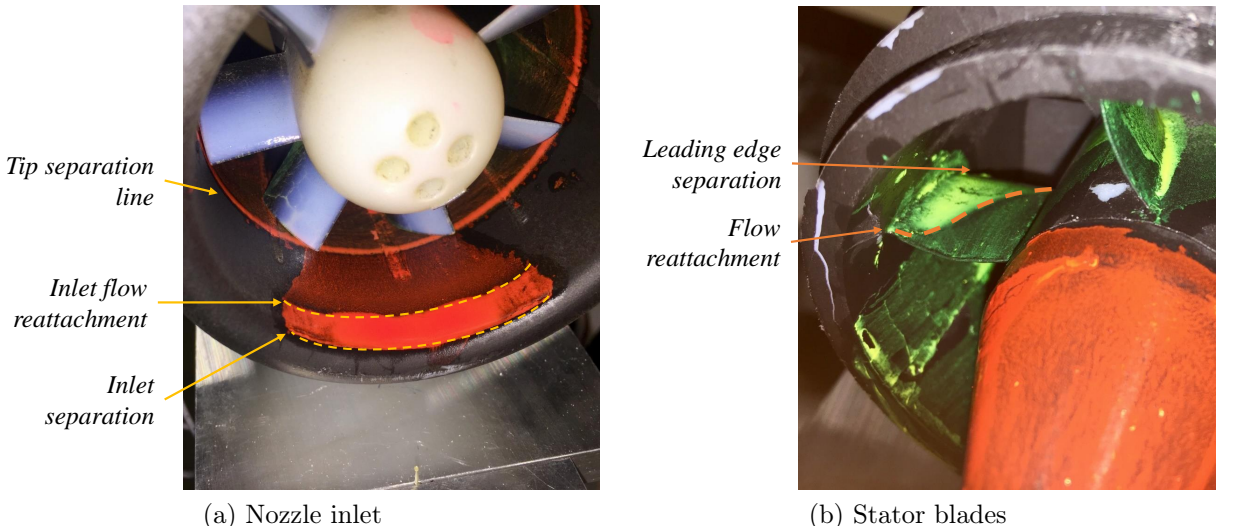


Figure 11: Flow visualisation of an initial design

The swirl velocity distribution is a function of the parameter n , such that:

$$V_\theta r^n = k \quad (37)$$

where $n = 1$ is a free vortex distribution and $n = -1$ represents a forced vortex distribution. Due to the low hub-tip ratio of the propulsor, the swirl velocity and stage loading distributions were chosen so as to reduce the loading near the hub. A value of $n = 0.1$ was used in the final design to reduce the stage loading near the hub where the camber is high (Fig. 12). Testing of an initial design, which assumed a free vortex swirl distribution showed that full-span separation at the leading edge was occurring and then partly reattaching (Fig. 11). This may have been due to a higher than predicted incidence onto the stator blades, end-wall and tip clearance effects, which were not accounted for in this model.

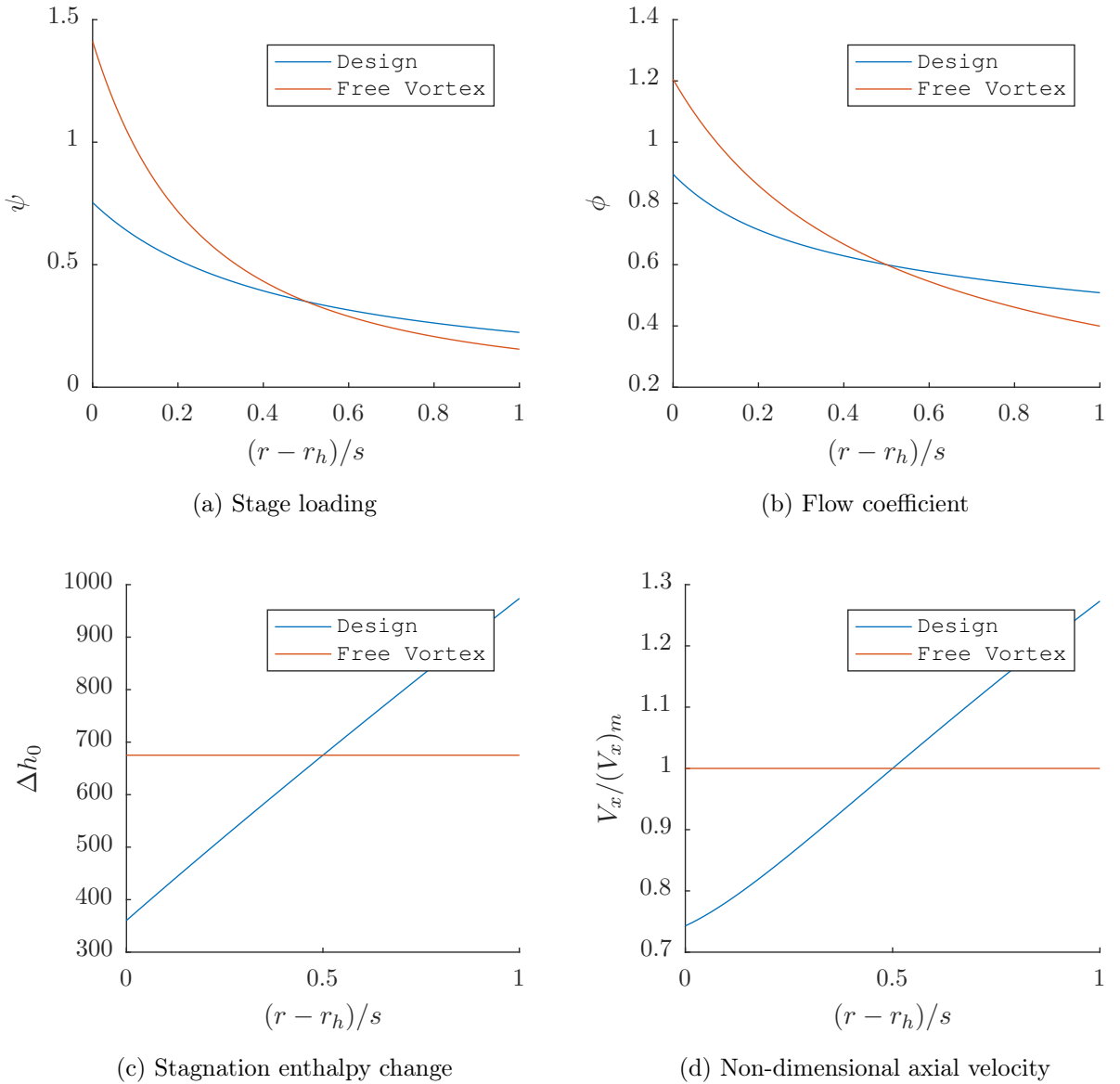


Figure 12: Flow and stage loading distribution across the blade span

For a given blade rotation rate, swirl velocity distribution, mean-line flow and stage

loading coefficients, the flow and stage loading coefficient distributions across the span can be determined by solving the *radial equilibrium equation* (Appendix C). For a given flow and stage coefficient distribution across the rotor span, the axial velocity and stagnation enthalpy change distribution can be found respectively. Subsequently, the mass flow rate and average stagnation pressure change across the rotor can be determined for a given isentropic efficiency. The isentropic efficiency of the propulsor (Eq. 38) was estimated from the testing of a initial design.

$$\eta = \frac{\Delta \bar{p}_0}{\rho \Delta \bar{h}_0} \quad (38)$$

Assuming isentropic flow and static pressure at the nozzle exit, continuity and Bernoulli's principle can be applied to determine the jet velocity, and hence the required nozzle ratio (NR). For a given inlet velocity, the propulsor thrust and power can then be evaluated using the steady-flow momentum and energy equations for the control volume shown in Fig. 2.

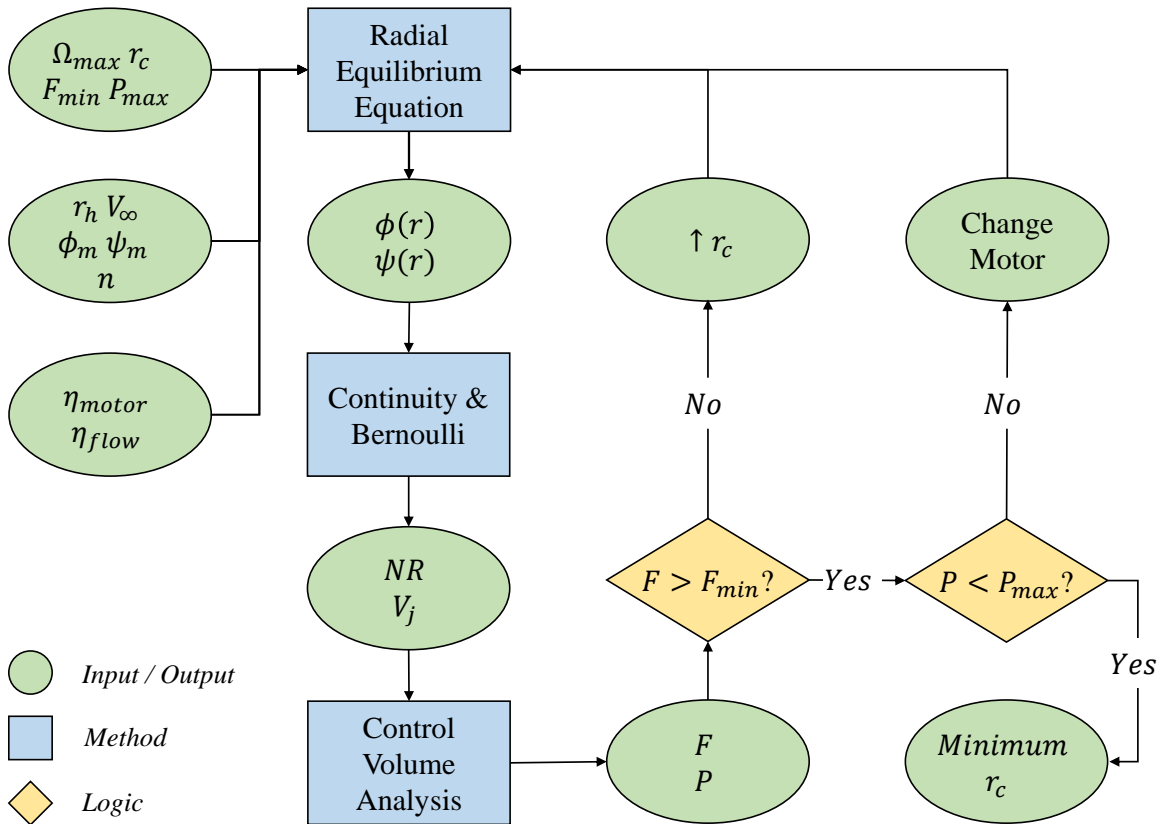


Figure 13: Flow diagram of the casing radius minimisation process

Step 2: Blade Number, Blade Metal Angles and Blade Geometry

The objective of the second step of the propulsor design is to determine the metal angles of the blade, which in turn can be used as inputs into a blade geometry script, which

computes the geometry of the rotor and stator blades. The design algorithm for calculating the blade metal angles is shown in Fig. 16. This design stage also required some additional inputs: the rotor and stator diffusion factors, and blade aspect ratios (Table 8).

Parameter	Value	Parameter	Value
Ω_{max}	18,000 rpm	AR_r	1
r_c	35 mm	AR_s	0.75
DF_r	0.45	DF_s	0.4

Table 8: Inputs for the detailed blade design algorithm

With the flow and stage loading distributions, hub and casing radius, and blade rotation speed determined from the previous step, and assuming axial inlet and exit flow, the relative and absolute angles at inlet and exit of the rotor and stator rows can be found (Fig. 14).

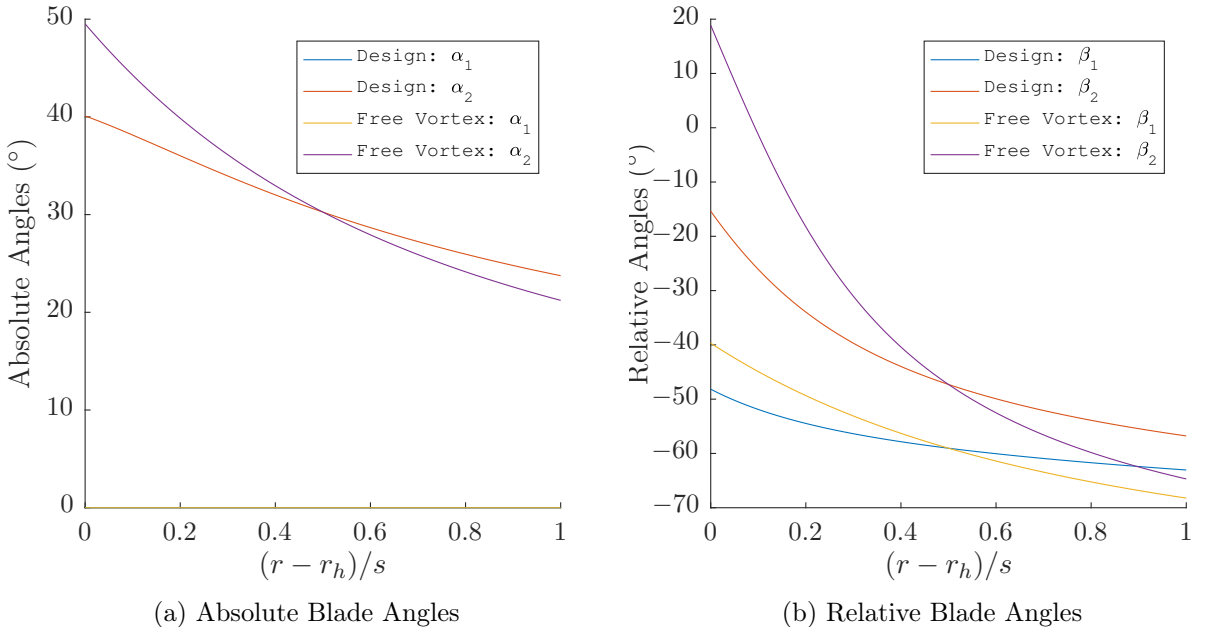


Figure 14: Comparison of absolute and relative flow angle distribution across the span for the $n = 0.1$ design and $n = 1$ free vortex design

Using the Lieblein empirical correlation for the Diffusion Factor (Eq. 39), the pitch-chord ratio can be found.

$$DF = 1 - \frac{\cos(\beta_1)}{\cos(\beta_2)} + \frac{1}{2} \cos(\beta_1) |\tan(\beta_2) - \tan(\beta_1)| \frac{l}{c} \quad (39)$$

The Diffusion Factor for commercial compressors is typically below $DF = 0.6$ to avoid separation. A $DF_r = 0.45$ and $DF_s = 0.4$ were selected for the rotor and stator respectively to avoid excessive loss in the stage due to separation. Maffioli [12] found that

at low Re this value of diffusion factor provides a good trade-off between efficiency and operating range.

The pitch-chord ratio and assumed blade aspect ratios (span-chord ratio) set the number of rotor and stator blades. The optimum aspect ratio may vary between 0.9 and 1.8 depending on the compressor design [15]. The mechanical requirement for the stator blades to be large enough to pass a hole through the blade centre for the motor wires set a limit on the maximum aspect ratio for the stators. Moreover, the maximum aspect ratio of the rotor blades was limited by the mechanical constraint that the trailing edge thickness of the rotor blades, t_{TE} , needed to be greater than 2 mm so that the 3D printed blades did not bend whilst rotating at or accelerating up to the design-speed. For the design, aspect ratios of $AR_r = 1$ and $AR_s = 0.75$ were selected.

The final step of the design was estimating the incidence and deviation onto the rotor and stator blades. The rotor blade deviation can be estimated using Carter's empirical relation [17]. Carter's correlation was designed for high Re , and as such is unlikely to provide accurate results, as research on low Re has shown greater deviation [12]. Nonetheless, the rule provided a useable estimate for the initial design. Testing of the initial propulsor then showed that the deviation angles were approximately twice as high as those predicted by Carter's rule.

The metal angles for the rotor and stator blades were calculated using the flow, deviation and incidence angles. The distribution of the metal angles across the span are shown in Fig. 15. The angles were then implemented into a blade geometry script developed for low Reynolds number compressors, which produced the coordinates of each blade section [20].

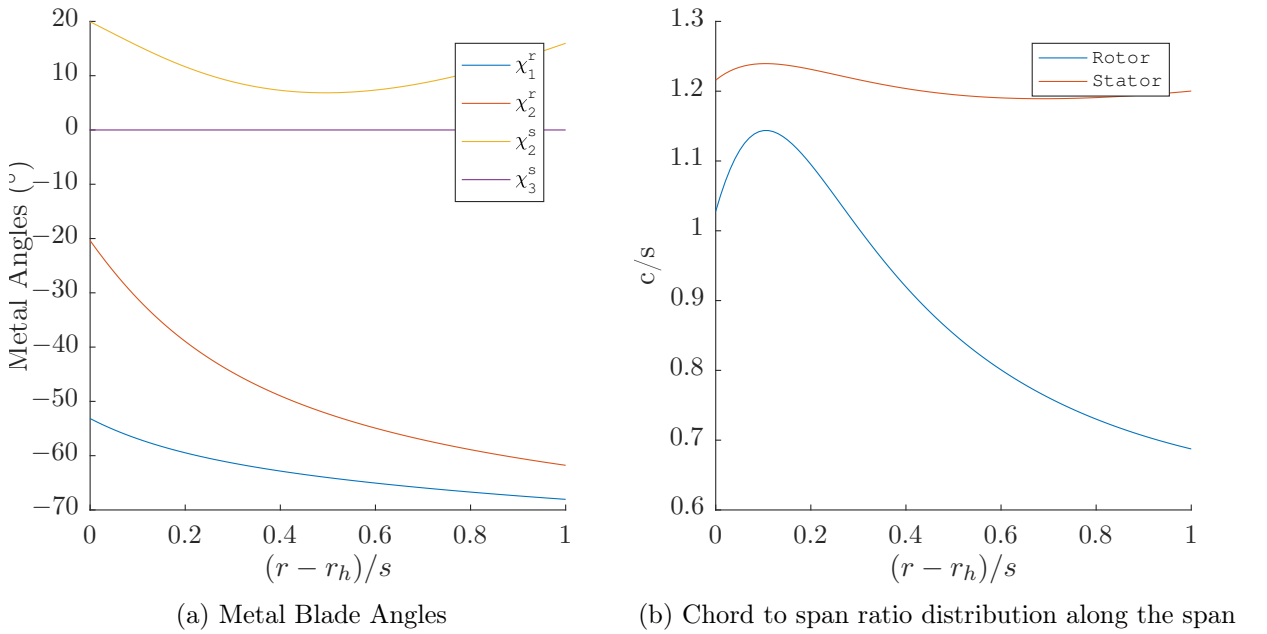


Figure 15: Blade metal angles and chord distribution along the span

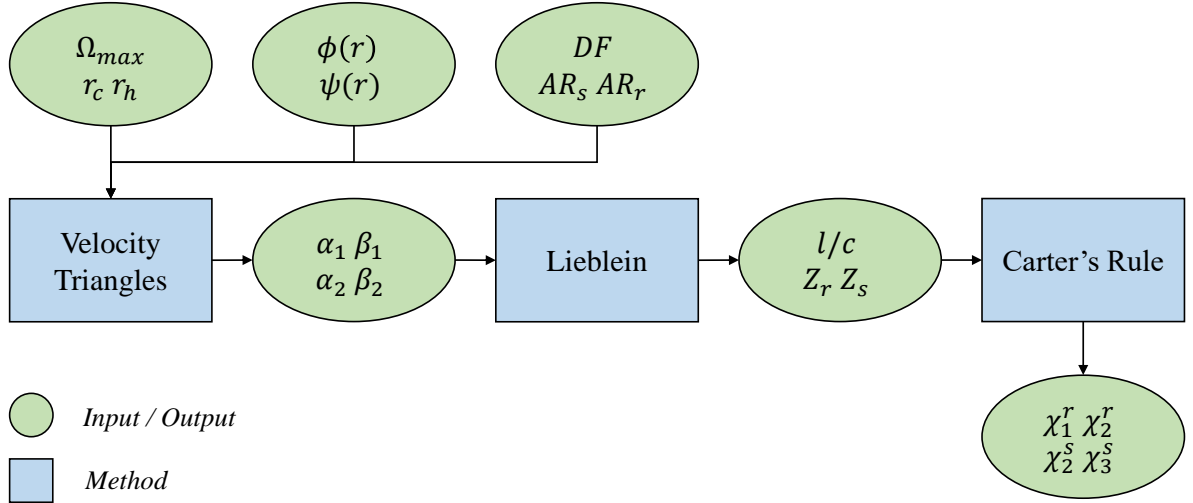


Figure 16: Flow diagram of the detailed blade design algorithm

Final Design

The final blade designs at the hub, mid-span and casing are shown in Fig. 17. The key parameters for the design point are shown in Table 9, while the detailed blade design results are listed in Appendix D.

ψ_m	0.35	Ω	18,000 rpm
ϕ_m	0.6	DF	0.40
Λ	83%	η_{is}	50%
F	1.57N	P_{motor}	86W

Table 9: Design point for axial compressor

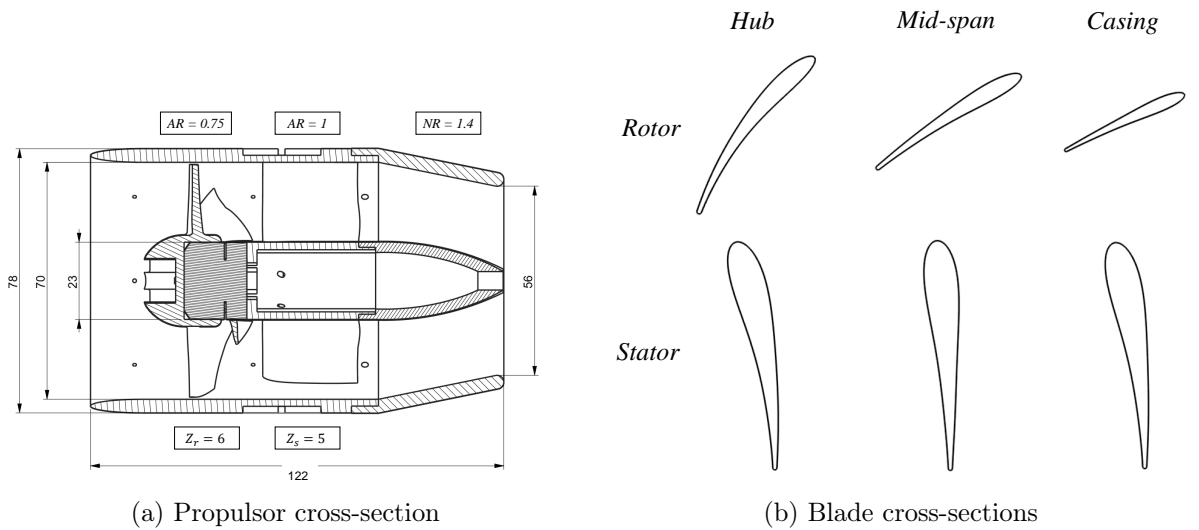


Figure 17: Propulsor cross-section

4 Results and Discussion

4.1 Aerodynamics of the Propulsor

Performance at the Design Point

The experimental and theoretical model results at the design operating point are shown in Table 10. The design point parameters were obtained from a discrete control volume analysis, as described by Cumpsty and Horlock [18], of the traverse grid at $x/L = 0.5$ downstream of the propulsor.

Parameter	Design	Experiment	Units
ψ	0.33	0.36	
$\bar{\phi}$	0.59	0.50	
η_{is}	50	45	%
V_j	33.9	31.3	m/s
\dot{m}	0.113	0.089	kg/s
F	1.57	1.33	N
P	86	61	W

Table 10: Design and experimental results at the design operating point

The propulsor runs at a flow coefficient below the design value, which leads to a lower mass flow rate and jet velocity at the nozzle exit. As such, the measured propulsor thrust and power of 15% and 29% respectively are lower than the values predicted by the model. The discrepancy between the results is two-fold: as the 2D propulsor model cannot handle the impact of 3D geometry effects, the impact of the rotor's tip clearance gap and end-wall boundary layer growth on the flow dynamics are not modelled. Additionally, the flow upstream of the rotor is distorted by the bypass flow through the motor's cooling system and reduces the mass flow rate through the blade passage.

At the hub and casing the local flow coefficient is lower than the design due to the effect of end wall boundary layer flows. This locally increases the incidence onto the rotor and stator blades, thus leading to a corner separation at the leading edge of the stator blades (Fig. 18). The reduction in the effective free stream, known as *blockage*, decreases the mean flow coefficient and mass flow rate through the propulsor.

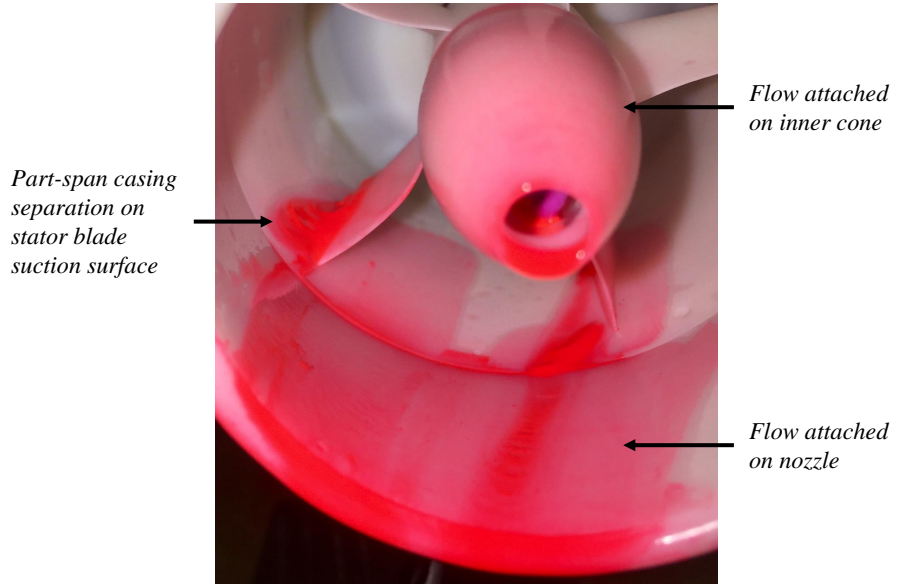


Figure 18: Flow visualisation of the stator blades, nozzle and inner cone of the propulsor at the design operating condition

The static and stagnation pressure within the propulsor were measured using a mid-height pitot-tube at inlet with static-pressure tappings on the casing at each section, shown in Fig. 10. The static pressure coefficient is defined as:

$$C_p = \frac{p - p_\infty}{p_{0,\infty} - p_\infty} \quad (40)$$

The theoretical model and experimental results both show a drop in the static pressure coefficient across the inlet. The measured static pressure coefficient rise across the rotor section, $\Delta C_p = 0.6$, was 92 % of the predicted value. However, the static pressure rise coefficient in the stator stage (sections 3 to 4) was lower at only 20 % of the predicted value. The model assumes that there is axial flow at the stator exit and an isentropic stagnation pressure change across the stators. The flow visualisation results confirm, however, that we would expect to measure a lower static pressure rise due to the flow separating and non-axial flow at the trailing edge of the stator blades. The static pressure then returns to atmospheric pressure, as one would expect for a subsonic propulsor.

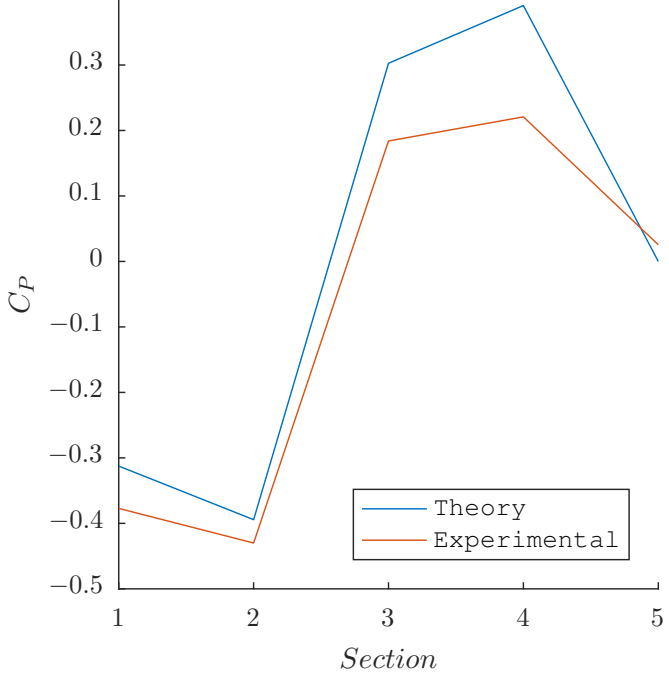


Figure 19: Static pressure coefficient along the propulsors' sections at the design operating condition

Traverse Results

Results from a traverse ($80 \times 80 \text{ mm}$; 2 mm increments) taken at $x/L = 0.5$ behind the nozzle exit at its design operating point ($Re = 1.5 \times 10^6$ and $\Omega = 18,000 \text{ rpm}$) are shown in Fig. 20.

The core velocity jet and a thin layer of entrained fluid can be seen in the non-dimensional axial velocity plot (Fig. 20 (a)). The location of the stator blades is also visible as the flow velocity in the stator wake is lower than the flow passing through the blade passage. The viscous losses in the wake also lead to a lower stagnation pressure coefficient downstream of the stators (Fig. 20 (b)). Five anti-clockwise rotating vortices can also be identified from the vorticity flow fields results (Fig. 20 (c)). These vortices are formed by flow separating on the suction surface of the blades. The flow from the higher pressure suction surface will be forced into the lower pressure region of the wake, thus creating flow circulation and vortices downstream of the trailing edge of the stator blades. An anti-clockwise rotating ring of vorticity is visible around the nozzle exit as well. This vorticity ring will have been induced by the shear between the clockwise rotating swirl of the jet flow and the axial external flow. The exit swirl is highest near the casing, which is where the flow separates (Fig. 20 (d)). Nearer to the hub, the swirl is approximately a third of that near the casing. The red patch of flow near the hub is where the swirl is approximately zero. As such, the stators seem to be performing closer to design here. The asymmetry of the could be due a non-zero incidence in the pitch at the inlet. This

would have been caused by the redirection of flow as a result of the wind-tunnel blockage from the mounting plate and load cell.

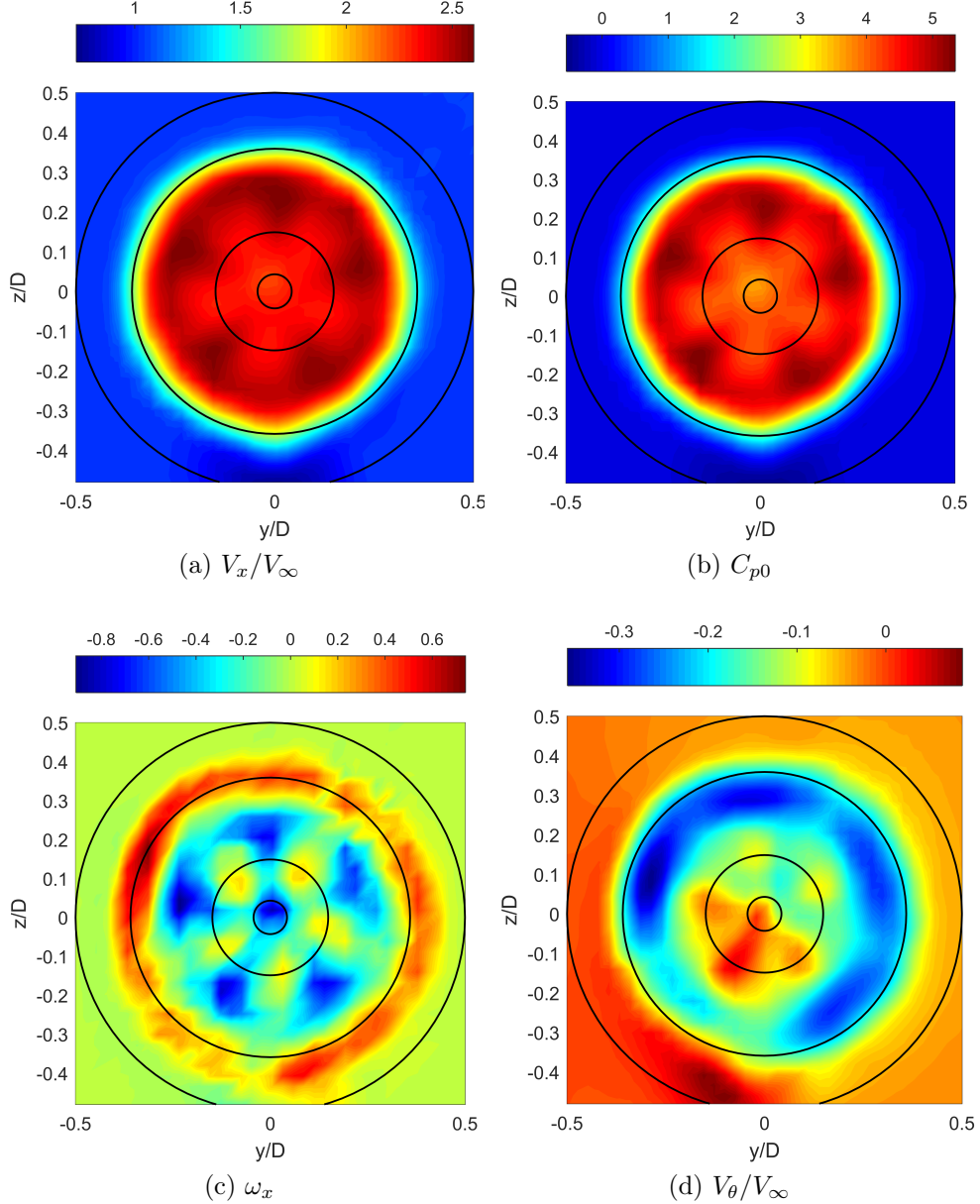


Figure 20: Traverse results downstream of the propulsor at the design point

The rotor blades were designed with an increasing axial velocity from the hub to casing along the span (Fig. 12), which is why an increasing flow coefficient is observable from the radially averaged results in Fig. 21 (a).

The radially averaged results for the deviation decrease in magnitude as the Reynolds number approaches the design operating point (Fig. 21 (b)). As the Reynolds number decreases and the compressor operates further away from its design operating point, the separation on the stator blades increases, which leads to a higher stator deviation. At the design-point, the maximum deviation of $\delta \approx 5.2^\circ$ occurs near the edge of the nozzle, which is as a result of the flow separating near the casing.

The circumferentially averaged stagnation pressure coefficient is shown in Fig. 21 (c) and is defined as:

$$C_{p0} = \frac{p_0 - p_{0,\infty}}{p_{0,\infty} - p_\infty} \quad (41)$$

The periodic change in the stagnation pressure coefficient is due to the wake formed downstream of each of the five blades. As the Reynolds number increases the stagnation pressure coefficient decreases. This is because the stagnation pressure rise across the rotor is a function of the stage loading, which does not scale with the inlet velocity squared.

The static pressure coefficient results similarly exhibit periodic behaviour due to the five stator blades (Fig. 21 (d)), but the periodicity is less well-defined than the stagnation pressure coefficient results.

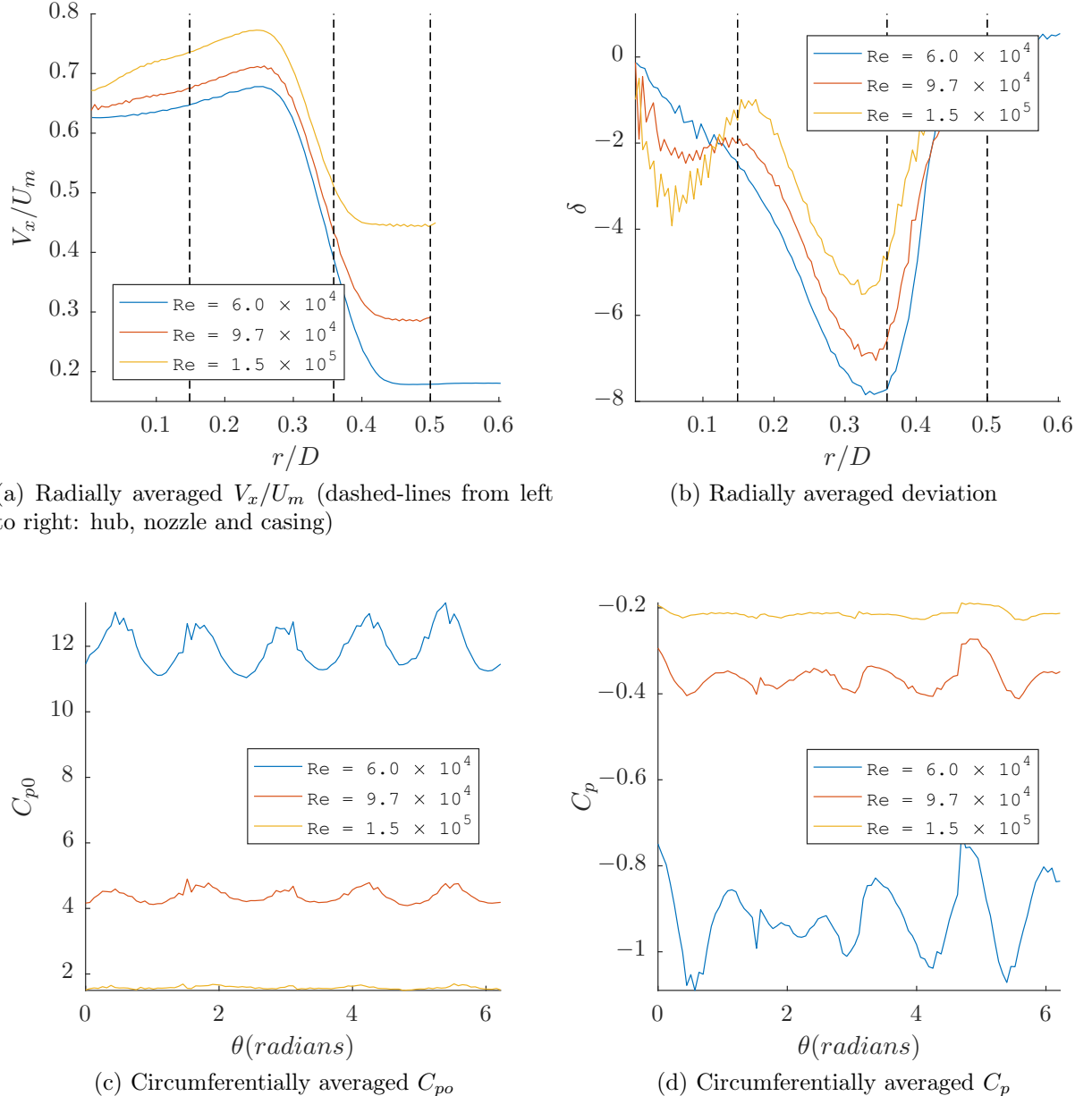


Figure 21: Radially and circumferentially averaged quantities for

Thrust and Power Characterisation of Propulsor

A calibrated load-cell and motor power-meter were used to measure the thrust and power of the propulsor as a function of the blade Reynolds number at static conditions ($V_\infty = 0$). The results from the experiment and theoretical model are shown in Fig. 22 (a). In order to meaningfully compare the model and experimental results, the measured stage loading and flow coefficients at the design blade Reynolds number ($V_\infty = 0$ and $Re = 7.85 \times 10^5$) were used as inputs into the model. The blade Reynolds number, thrust coefficient, and non-dimensional power (i.e. Newton number) are defined as follows:

$$Re = \frac{\Omega D^2}{\nu} \quad (42)$$

$$C_F = \frac{F}{\frac{1}{2}\rho U_m^2 D^2} \quad (43)$$

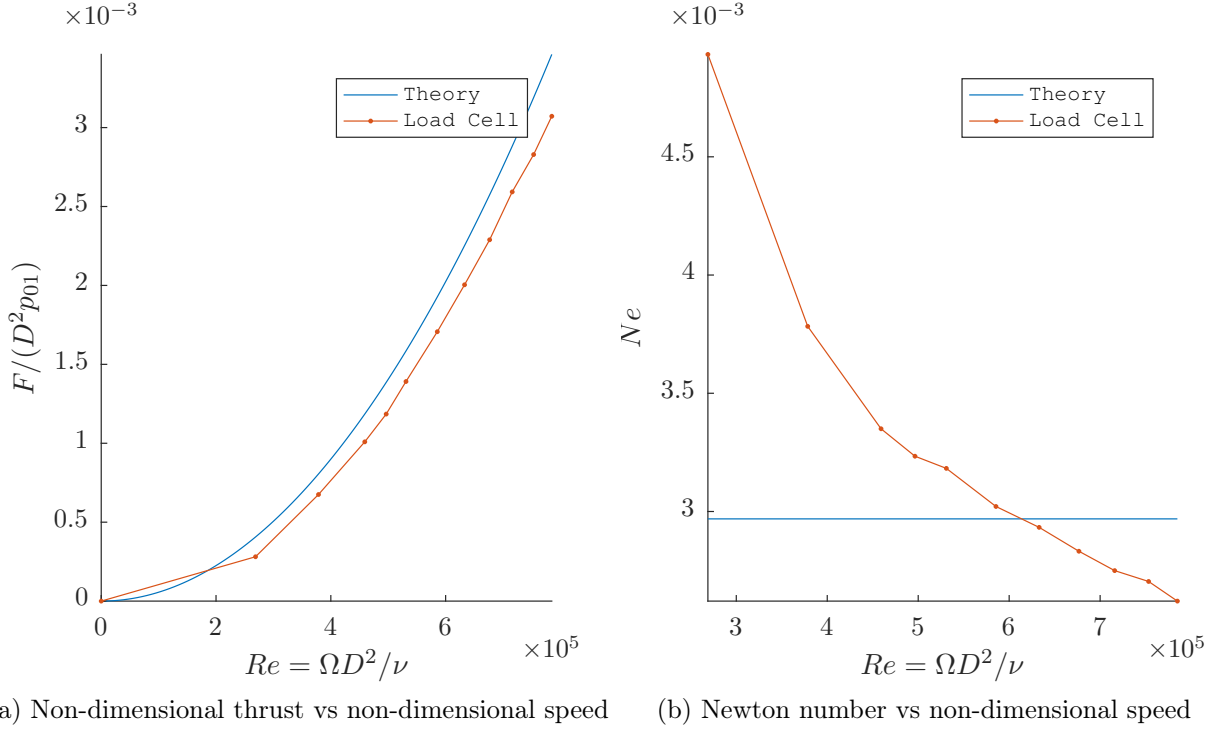
$$Ne = \frac{P}{\rho \Omega^3 D^5} = f(\phi, Re) \quad (44)$$

where D is the inlet diameter.

The theoretical model assumes a constant flow and stage loading coefficient at all blade Reynolds numbers. For the range of blade Reynolds numbers considered, the experimental and theoretical results agree to within a percentage error of 9.4 %.

The input power was also measured using the motor's power meter as a function of the blade rotation speed. The results are plotted non-dimensionally in Fig. 22 with Newton number, a non-dimensional form of the compressor input power, against the blade Reynolds number. For a compressor with a fixed nozzle ratio, the Newton number is a function of the stage loading and flow coefficient. The theoretical model assumes that both coefficients and the motor efficiency are constant. As such, the Newton number is independent of the Reynolds number.

The experimental results indicate that the Newton number decreases as the Reynolds number is increased. We would expect that as the blade Reynolds number is increased, the viscous effects reduce and hence the Newton number decreases. Moreover, as the propulsor operates closer to its design operating speed, we would expect the flow coefficient to increase and the blockage to reduce. However, a variation of 37 % due to these effects is larger than expected. It is possible therefore that the efficiency of the motor is increasing with the blade rotation speed, although this was not examined further due to the lack of a detailed motor characteristic.



(a) Non-dimensional thrust vs non-dimensional speed (b) Newton number vs non-dimensional speed

Figure 22: Static test thrust and power vs blade rotation speed of the propulsor

Change in Thrust with Inlet Velocity

BLI theory shows that for an idealised propulsor, the propulsive efficiency decreases with higher inlet flow velocity (Section 2.2). We therefore expect that as the wind-tunnel Reynolds number increases for a given input power, the propulsive efficiency, and in turn the thrust coefficient, decreases. The wind-tunnel Reynolds number is defined as:

$$Re = \frac{V_\infty L}{\nu} \quad (45)$$

where L is the length of the propulsor.

The net thrust of the propulsor was calculated experimentally using a load cell and by traversing the flow downstream of the propulsor. The thrust was measured using the load cell when the motor was switched off and when the motor was operating at design-speed. The net thrust was then estimated as the difference between the total force (i.e. motor on) and the drag (i.e. motor off). It is therefore assumed that the assembly drag is independent of whether the motor is on or off. The net thrust from the traverse is obtained from a control volume analysis of the downstream and upstream flow, as described by Cumpsty and Horlock [18].

The model assumes constant stage loading and flow coefficients. In order to compare the theory and experimental measurements, the coefficients used in the model were those measured at the design wind-tunnel Reynolds number ($Re = 1.5 \times 10^5$).

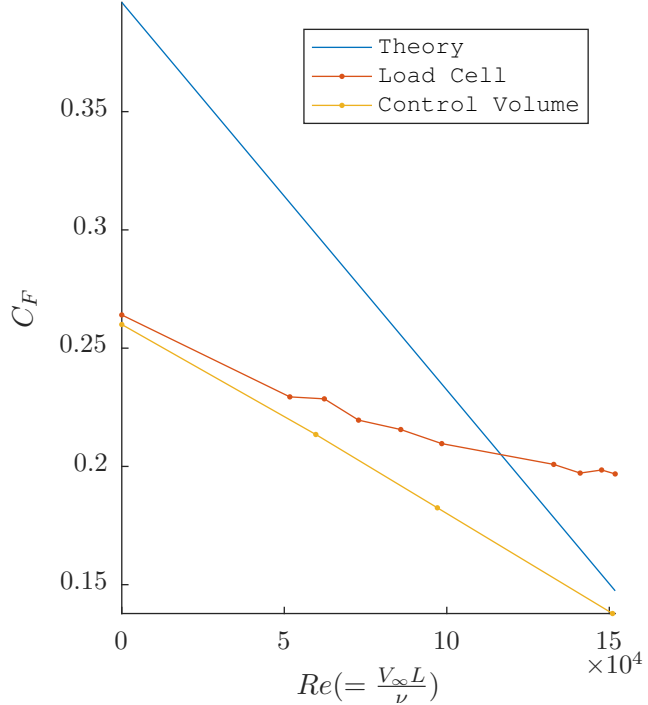


Figure 23: Thrust coefficient vs wind-tunnel Reynolds number

The thrust coefficient measurements from the load cell and traverse results diverge as the Reynolds is increased. This is because of the effect of the entrainment of flow through the propulsor on the drag coefficient of the assembly, which invalidates the assumption that the drag is independent of the propulsor at higher Reynolds numbers.

As the Reynolds number increases, the theoretical model results more closely align with the experimental measurements. This is because at the design operating point, the flow and stage loading coefficients are matched. However, as the Reynolds number is decreased, the real propulsor operates away from its design point, leading to a decreasing flow coefficient and mass flow rate, which the model does not capture.

The theoretical model predicts a linear decline in the thrust coefficient as the Reynolds number is decreased. This is because for a fixed blade rotation speed and flow coefficient, the mass flow rate, and in turn the jet velocity, are fixed. As such, the thrust coefficient decreases linearly with the Reynolds number according to Eq. 48.

$$F = \dot{m}(V_j - V_\infty) \quad (46)$$

$$C_F = \frac{-\dot{m}V_\infty}{\frac{1}{2}\rho U_m^2 D^2} + const \quad (47)$$

$$\therefore C_F = \gamma \times Re + const \quad (48)$$

where $\gamma \propto \dot{m}$.

The rate of change of the thrust coefficient with the Reynolds number from the exper-

imental results is 56 % lower than the theoretical results. This is due to the change in flow coefficient as the propulsor operates off-design and the nozzle is then no longer matched to the operating condition, thus causing the isentropic efficiency to decrease further.

4.2 Aerodynamics of the Hybrid Airship Assembly

Traverse Results

Traverses were conducted downstream of the airship hull at $x/L = 0.4$ and $x/L = 1$ (where L is the airship length) in order to measure the development of the flow field in the axial direction. The results for the stagnation pressure coefficient and vorticity are shown in Figures 24 and 25. The flow is viewed along the negative x axis (i.e. from downstream to upstream).

The airship design is symmetric about the horizontal and vertical planes. As such, at a zero angle of attack we would expect the stagnation pressure coefficient to be symmetrical about the horizontal and vertical centre lines. The traverse results for the stagnation pressure coefficient are symmetrical about the y plane (vertical), but asymmetrical in the z plane (horizontal) (Fig. 24). The asymmetry in the horizontal plane is due to the fairing around the pylon on the bottom surface of the airship. The interaction between the flow around the fairing and airship leads to a greater stagnation pressure loss near the lower surface. Further downstream of the airship, the results show that the stagnation pressure coefficient in the trailing wake has increased, which is due to the dissipation of the streamwise kinetic energy in the trailing wake: $\dot{E}_a \rightarrow \Phi_w$ (Eq. 8).

A vertical line of stagnation pressure loss due to the separation of the flow near the trailing edge of the fairing can also be observed further down and away from the airship's hull.

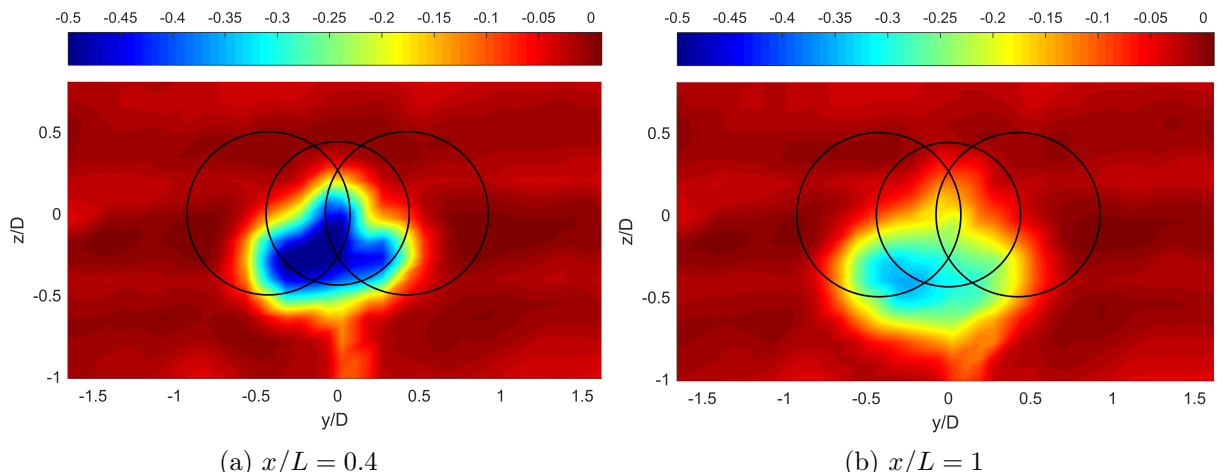


Figure 24: C_{p0} downstream of the airship

The flow vorticity, $\vec{\omega} = \nabla \times \vec{v}$ of the flow field is calculated using the Forward Euler

method [26]:

$$\omega_x = \frac{\partial v}{\partial z} - \frac{\partial w}{\partial y} \quad (49)$$

$$\omega_x^n \approx \frac{v^{n+1} - v^n}{\Delta z} - \frac{w^{n+1} - w^n}{\Delta y} \quad (50)$$

In Fig. 25 (b) two Rankine vortices can be observed. The left (blue) vortex is rotating in the clockwise direction, while the right vortex (red) is rotating in the anti-clockwise direction. The asymmetry of the aircraft wake leads to a pressure imbalance on the upper and lower surfaces, which has caused the two counter-rotating vortices to form. This pressure differential forces the flow to be convected from the upper to lower surface. The existing flow on the lower surface is then pushed outwards and upwards around the side by the incoming flow, thus generating the two inward counter-rotating vortices.

Downstream of the trailing edge, the wake formed by the airship has expanded downwards and to the side as a result of the flow distribution due to the swirl induced by the vorticity. The mutual interaction of the counter rotating circulating velocity fields of each vortex also induces a negative z velocity component, which causes the vortices and the wake (Fig. 24 (b)) to shift downwards.

In Fig. 25 (a), two smaller counter-rotating vortices, which are rotating outward, are also visible. Given their location and direction of rotation, they appear to be formed by the horseshoe vortices that can be seen in the flow visualisation results between the fairing and the airship (Fig. 26).

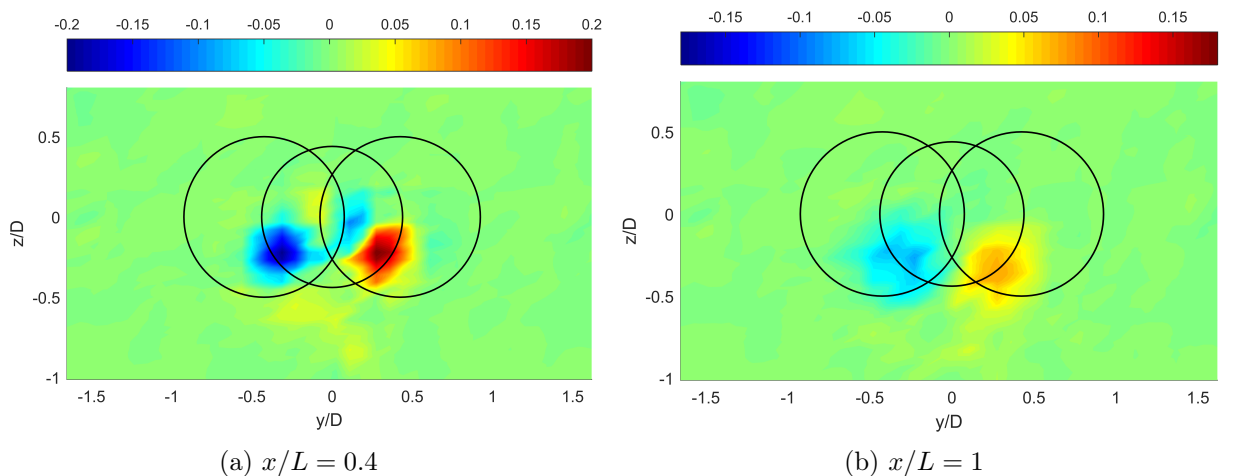


Figure 25: ω_x downstream of the airship

Flow Visualisation Results

The asymmetry of the results in the z plane is due to the interaction of the fairing and the airship. The unstable nature of the flow on the lower surface meant that the flow was very sensitive to any tip-gaps or misalignments in the airship or fairing. The flow visualisation results indicate that the flow was separating earlier on the lower surface, which explains why there is a larger stagnation pressure loss there (Fig. 26 (a)).

Flow visualisation of the fairing was conducted to verify the simulation results from the 2D viscous solution of the fairing airfoil (Fig. 26). The *XFOIL* results (Fig. 6) predict a laminar separation bubble and consequent reattachment following transition to turbulence. The flow visualisation identifies the points of laminar separation, turbulent reattachment and turbulent separation. The location of the laminar separation occurred earlier than the *XFOIL* results predicted. Moreover, *XFOIL* was unable to correctly predict the location of the turbulent trailing edge separation. The differences between the experimental and computed results are due to the lower tolerance of the flow to the rough surface of the fairing at low Reynolds numbers.

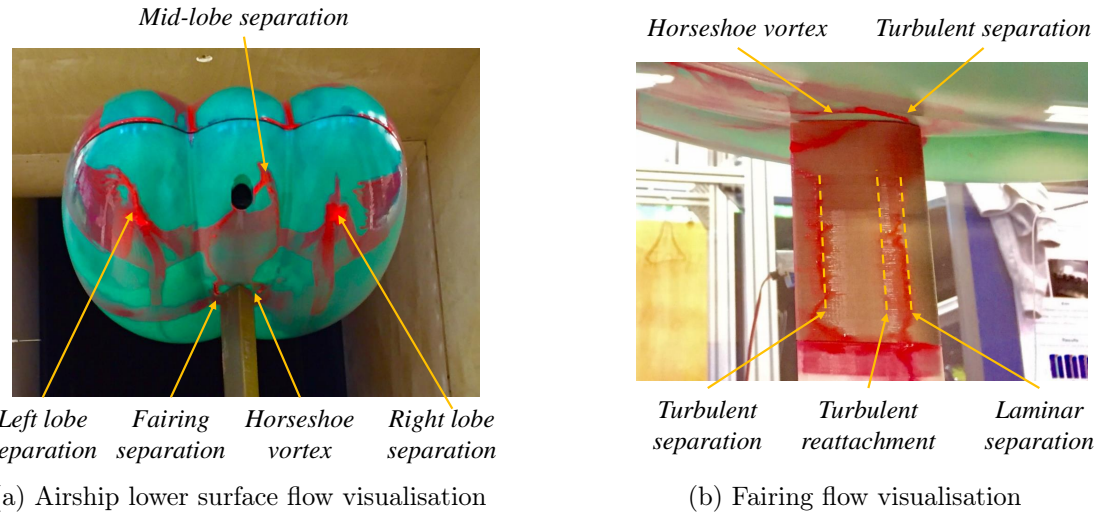


Figure 26: Flow Visualisation Results for the Airship

Drag Coefficient

The drag coefficient of the hybrid airship was calculated using experimental results from the load-cell and a control volume analysis of the hybrid airship. The results are compared with those from the theoretical model for the drag coefficient (Eq. 35) at a zero degree of angle attack (Fig. 27).

The drag coefficient calculated from the control volume analysis exceeds that of the load cell measurements by approximately $\Delta C_D \approx 0.01$. The discrepancy between the two results is due the drag of the fairing, which is included in the control volume analysis but not in the load cell drag coefficient measurement. The drag coefficient (Eq. 31) of

the airfoil was calculated to be $C_D = 0.003$. However, this value was calculated for a 2D airfoil with flow attached at the trailing edge. The real fairing is subject to 3D interaction effects between the airship and the fairing, as well as flow separation near the trailing edge.

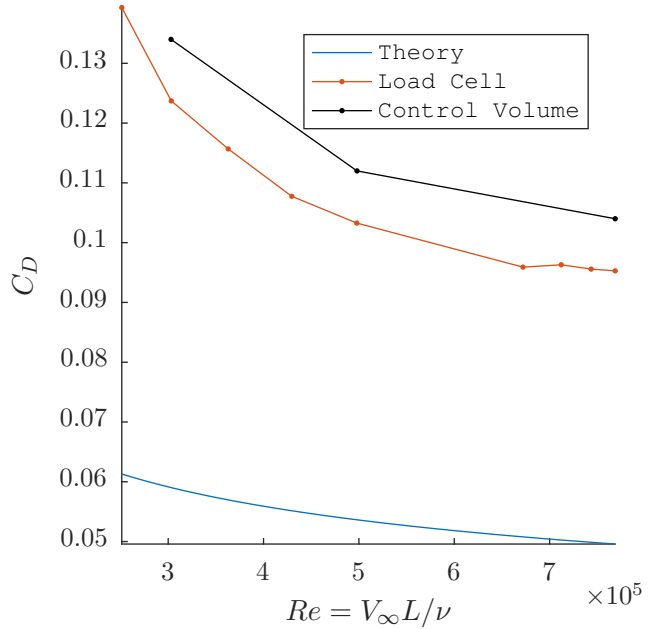


Figure 27: Drag coefficient of the hybrid airship hull as a function of the Reynolds number

The theoretical model and experimental results differ by $\Delta C_D \geq 0.045$, a percentage difference of over 50%. The theoretical model is strictly applied to 2D streamline bodies, so 3D drag effects such as induced drag as a result of pressure differentials between the upper and lower surfaces were not accounted for in the model. Moreover, the flow visualisation and traverse results have shown that the fairing has had a significant affect on the flowfield's symmetry and the size of the wake formed, which the model did not account for. If the flow field on the upper surface is mirrored on the horizontal centre-line and the control analysis repeated, the percentage difference between the results is reduced to 8%, thus quantifying the impact that the asymmetry has had on the drag coefficient measurements.

4.3 Impact of Boundary Layer Ingestion on the Hybrid Airship's Performance

Traverse Results

Traversing of the airship's hull showed that the flowfield was symmetrical about the vertical centreline of the airship. As such, half-traverses of the right-hand-side only for the non-BLI reference (Fig. 29 (a)) and BLI cases (Fig. 28 (a)) were conducted downstream

of the airship and propulsors. The thrust of the propulsors was increased until the load cell recorded a zero net force. The input power for each propulsor was then recorded at the beginning and end of each traverse and the average value was used to calculate the PSC (Eq. 1).

Figures 28 (b) and 29 (b) focus on the stagnation pressure downstream of the propulsors. The results hint at a more distorted stagnation pressure distribution for the BLI case. This was investigated by Plas et al. [1], who similarly found that the ingestion of the wake led to distortion of the static and stagnation pressures at the exit of a fan. As the distortion transfer becomes worse, the blockage in the fan can increase, thus leading to more work being required to reach the desired net thrust. Distortion effects can therefore negate the benefits of BLI.

The average stagnation pressure coefficient in the propulsor jet is lower for the BLI than the non-BLI case (Fig. 30). This is because the boundary layer ingesting propulsion system is re-energising the airship's wake and accelerating flow with a lower inlet kinetic energy. The jet velocity of the propulsor is therefore lower and the propulsive efficiency higher.

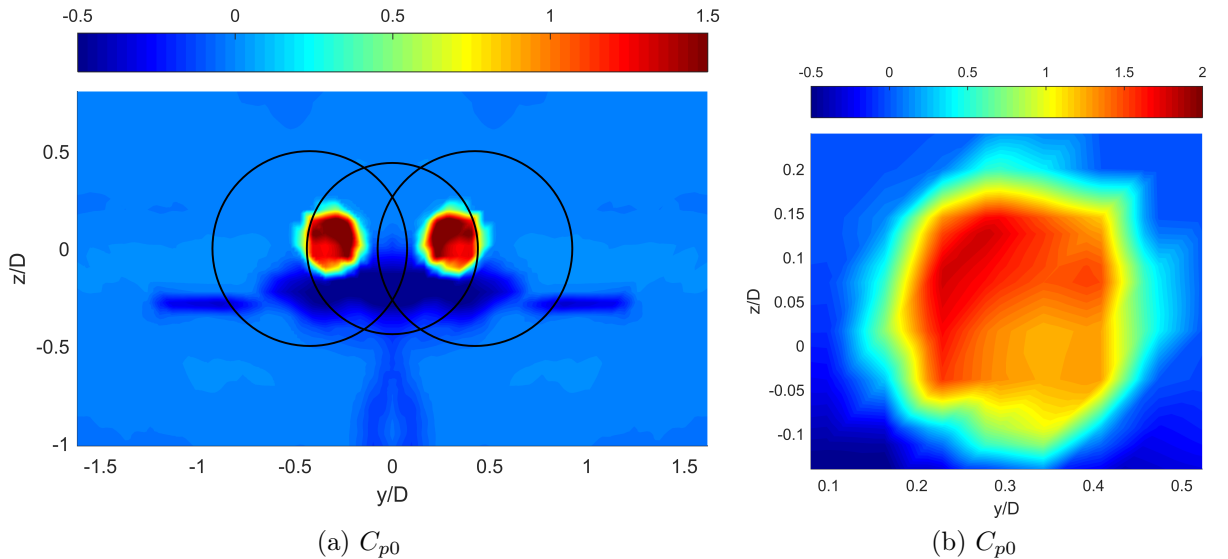


Figure 28: Traverse results for BLI case

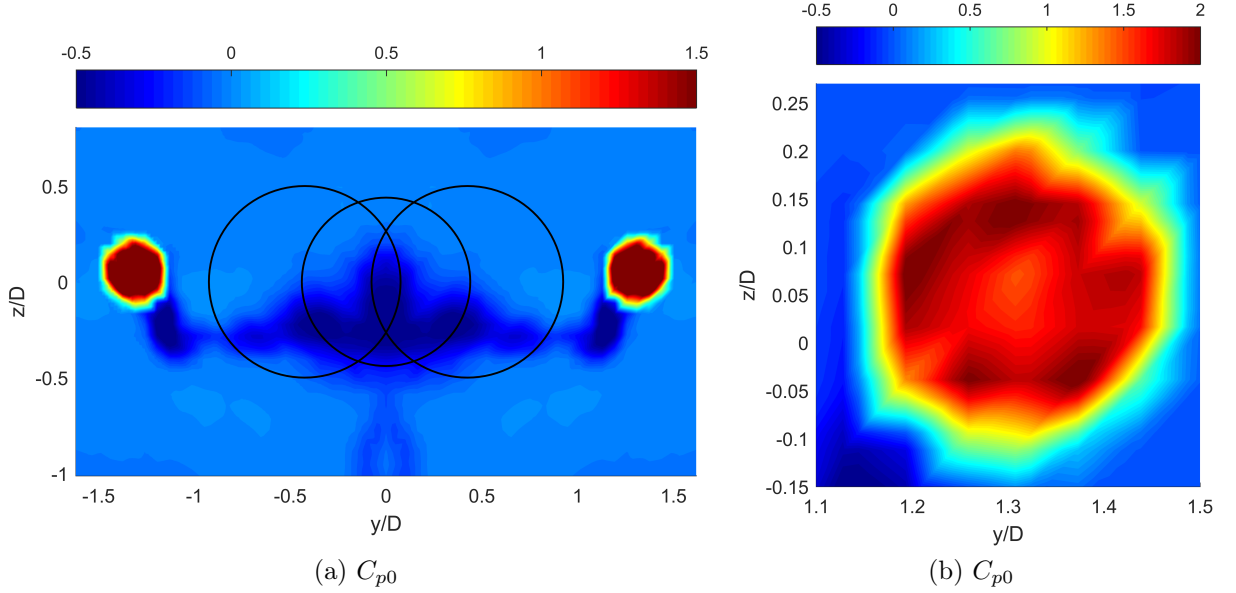


Figure 29: Traverse results for non-BLI case

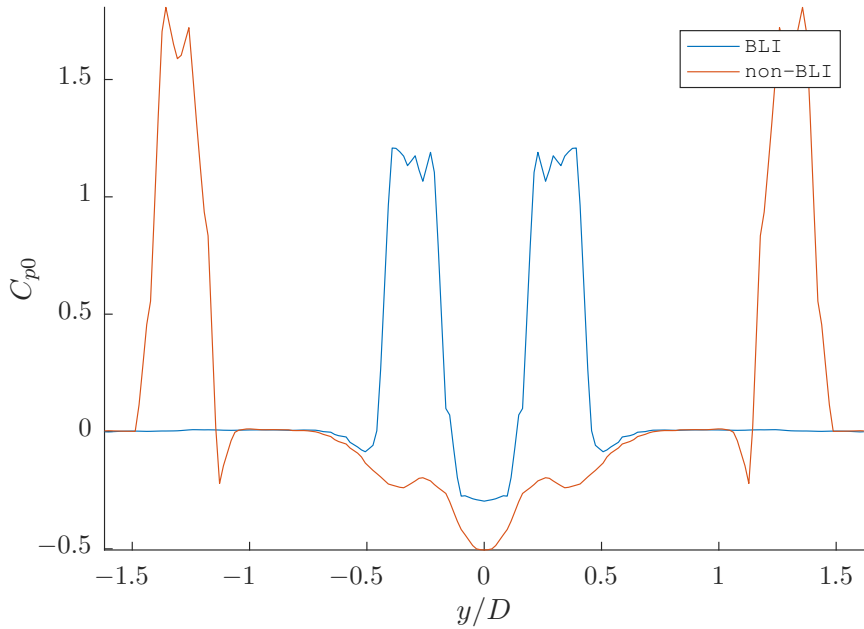


Figure 30: C_{p0} along propulsor centre-line

Force Corrections

Three wires connecting the motor to the power source were wrapped along the rear assembly and passed through the hull of the airship. Consequently, the total drag of the rear assembly was different for the two test cases as a result of the additional wiring required for the non-BLI versus the BLI case (Fig. 31). Note the axis in Fig. 31 has been scaled to highlight the tail assembly loss. In order to account for the extra thrust that

the propulsors in the non-BLI case had to produce to balance the additional wire drag, the power balance approach (Section 2.3) was applied to a control volume enclosing the wake formed by the wires. Since the flow is approximately adiabatic and there is no shaft work, the change in mechanical power, $\dot{m}\Delta p_0$, is equal to the dissipation due to the wires and the rear assembly, as well as the mixing losses that have occurred downstream in the wake.

$$\Phi_s + \Phi_w = -\dot{m}\Delta p_0 \quad (51)$$

Drela [6] showed that for a 2D object, the total mechanical power dissipation is equal to the force times the freestream velocity. Since the horizontal velocity component for the control volume is approximately zero, it is reasonable to assume that 3D flow effects are negligible. The extra drag is given by:

$$F_{error}V_\infty = -\dot{m} \sum_{i,j} \Delta(p_0)_{i,j} \quad (52)$$

Using a power-thrust characteristic for the propulsor, the reference non-BLI power can be adjusted to account for the net thrust error between the different BLI cases. A percentage error of 8 % was estimated for the reference (non-BLI) power.

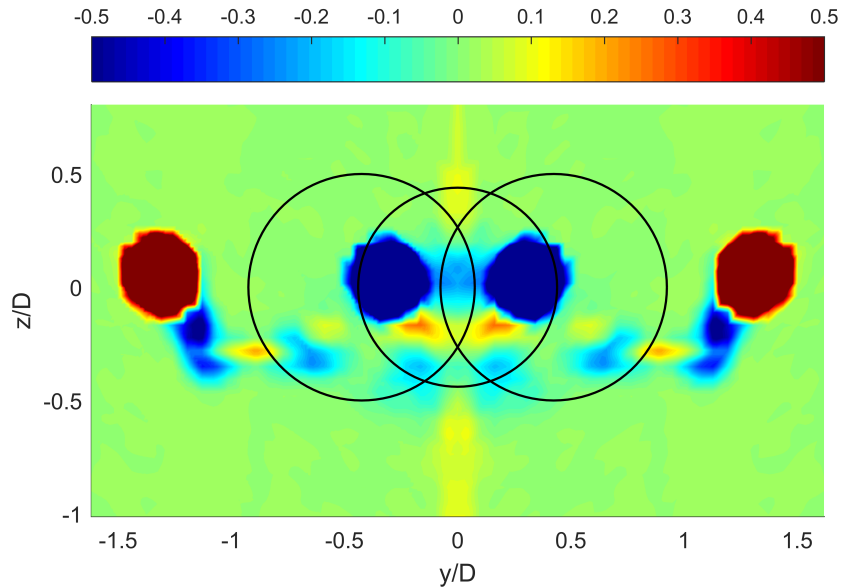


Figure 31: Difference in stagnation pressure coefficient between the BLI and non-BLI cases

Power Saving Coefficient

The power saving coefficient experimental results for the three traverses conducted are shown in Fig. 4 with the correction due to the thrust error applied. The experimental results are compared with the analytical results, which are obtained using the BLI model

in Section 2.3. The model uses the experimentally measured velocity flow-field from the traverse of the airship’s hull to calculate the expected PSC distribution as the propulsor’s horizontal position is changed (Eq. 19).

The experimental results show a maximum $PSC = 9.8\%$ at the propulsor location nearest to the centre-line. The analytical model similarly predicts that the maximum PSC is located at the centre-line and decreases as the propulsor moves outwards. Based on BLI theory alone, we expect the maximum benefit from BLI to occur when the propulsors are ingesting the maximum momentum deficit possible as this would reduce the net drag, and in turn the net thrust, of the propulsor. From the traverse of the airship’s hull (Fig. 24), the wake is largest near the vertical centre-line. As such, we would expect that the maximum PSC would be found near there.

While the range of data points is limited and further investigation of the experimental error is required, the preliminary results would appear to indicate that the optimum location for the propulsors would be as close to the centre-line as possible.

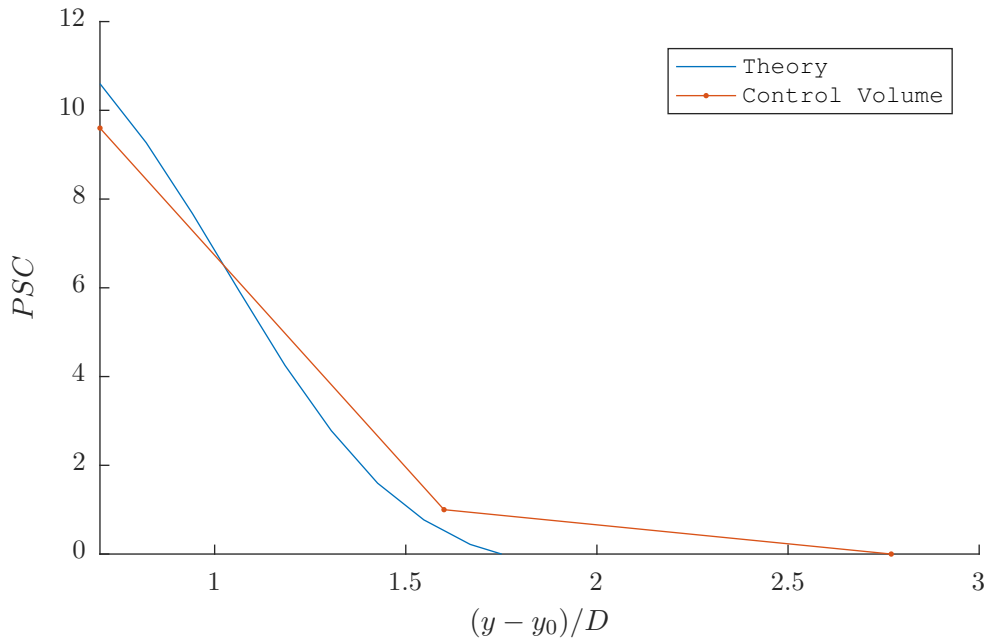


Figure 32: Power Saving Coefficient vs horizontal propulsor position

Conclusions

1. The propulsors successfully met the design objective of producing sufficient thrust to balance the drag of the airship despite the propulsors performing at a lower flow coefficient than the design model had predicted. This was due to the separation of flow at the stators, which occurred due to 3D flow effects that were not modelled in the 2D propulsor design.
2. A scale model airship was designed and manufactured to replicate the *Airlander 10*. Due to the unexpected sensitivity of the flow field to the interaction between the fairing and the airship, the symmetry of the airship flow field could not be reproduced in the horizontal plane. This consequently led to discrepancies between the theoretical and experimental results for the airship drag.
3. The results from the propulsor traverses were able to successfully resolve the vorticity and stagnation pressure coefficient flow fields. Precise measurements of the flow field could be made and matched up closely with the load cell results, thus allowing the key operating parameters to be calculated. The static pressure coefficient rise of the rotor was also 91% of the design value and the mean flow coefficient was 18% below the design value.
4. The design and manufacture of an experiment to explore the benefits of boundary layer ingestion effectiveness for a hybrid airship was completed and tested. Changes in the PSC for three cases were observed and the trend in the results closely matched up with the theoretical model's predictions. Additionally, the model was able to replicate the trends in the PSC with shape factor also observed by Smith [8].
5. The effect that the wires would have on the drag, and hence the accuracy of PSC measurement, were not expected. Nonetheless, by correcting for the effect using the power balance theory, the preliminary experimental results showed that a PSC of up to 9.8% could be achieved with the propulsors located nearest to the centre-line.

4.4 Future Development

The traverse and flow visualisation results of the hybrid airship demonstrated the extent to which the fairing has an effect on the symmetry of the flow. A redesign of the fairing or an alternative method for fixing the airship in place and measuring the force should therefore be considered in order to more accurately replicate the airship flow field. Moreover, experiments with a tripped flow should be considered given the high Reynolds number of the full-scale *Airlander 10*.

It was also evident from the traverse results for the two extreme BLI cases that the drag of the assembly was not equal for both cases due to the increased stagnation pressure

loss as a result of the wiring. An improved design should consider redesigning the rear assembly so that the stagnation pressure loss due to the wires is either constant or zero. Additionally, the rear assembly was not designed aerodynamically, which led to a wake forming behind the assembly and altering the flow field of the airship. The decoupling of the propulsors from the airship should possibly be considered to isolate the thrust and drag measurements for the flow. However, the balancing of the drag and thrust may be more difficult.

The effects of inlet distortion on the aerodynamics of the propulsor were only briefly discussed in this report, but present an interesting area of research. As such, if time had allowed, higher fidelity traverses of the upstream and downstream flow field of the propulsor could have been conducted.

Appendices

A Steady-Flow Momentum Equation of a Propulsor

$$\dot{m}_{in} = \dot{m}_{out} - \dot{m}_l \quad (53)$$

where \dot{m}_l is defined as the entrainment of mass flow into the lateral surfaces, S_l . Separating the air that flows through the engine and that external to the engine, we have:

$$\dot{m}_{in} = \dot{m}_a + \dot{m}_{in,ext} \quad (54)$$

$$\dot{m}_{out} = \dot{m}_a + \dot{m}_{out,ext} \quad (55)$$

Assuming that the streamlines entering the control volume are approximately horizontal, the corresponding momentum entering the control volume can be approximated by:

$$\int_{S_l} \rho(\mathbf{V}_1 \cdot \mathbf{x})(\mathbf{V}_1 \cdot \mathbf{z})dS \approx V_1 \int_{S_l} \rho(V_l \cdot n)dS = \dot{m}_l V_1 \quad (56)$$

where \mathbf{V}_1 is the velocity through the upper and lower surfaces of the control volume.

From this equation and the SFME we can obtain a simple equation for the thrust:

$$F = (p_2 - p_1)A_2 + \dot{m}_a V_2 + (\dot{m}_{out,ext} + \dot{m}_l - \dot{m}_{in})V_1 \quad (57)$$

$$F = \dot{m}_a(V_2 - V_1) + (p_2 - p_1)A_2 \quad (58)$$

If the velocity at the exit of the propulsor is subsonic (i.e. the nozzle is not choked), then $p_e \approx p_a$. Hence, the thrust equation is given by:

$$F = \dot{m}_a(V_2 - V_1) = \dot{m}_a \Delta V \quad (59)$$

$$F = \rho A_2(V_1 + \Delta V) \Delta V \quad (60)$$

For a constant propulsor nozzle exit area and thrust, Eq. 60 can be re-arranged to show that the change in flow speed through the propulsor is a function of the freestream velocity only.

$$\Delta V = -\frac{V_1}{2} \pm \frac{\sqrt{V_1^2 + 4k^2}}{2} \quad (61)$$

where $k^2 = \frac{F}{\rho A_2}$.

For an idealised isentropic propulsor, the shaft power is given by:

$$P = F \left(V_1 + \frac{\Delta V}{2} \right) \quad (62)$$

B Thrust and Net Thrust Analysis

For a propulsor located in the wake of an aircraft at cruise condition, the net drag must balance the net thrust for the combined control volume A and B in Fig. 3.

$$\dot{m}_{out,ext}(V_\infty - V_w) = \dot{m}_a(V_j - V_\infty) \quad (63)$$

The propulsor thrust is given by,

$$F_1 = \dot{m}_a(V_j - V_w) \quad (64)$$

For a propulsor located outside the wake of an aircraft at cruise condition the propulsor thrust is given by:

$$F_2 = \dot{m}_{a,2}(V_{j,2} - V_\infty) = \dot{m}_{out}(V_\infty - V_w) \quad (65)$$

where $\dot{m}_{out} = \dot{m}_{out,ext} + \dot{m}_a$

$$F_2 = (\dot{m}_{out,ext} + \dot{m}_a)(V_\infty - V_w) \quad (66)$$

$$F_2 = \dot{m}_a(V_j - V_\infty) + \dot{m}_a(V_\infty - V_w) \quad (67)$$

$$F_2 = \dot{m}_a(V_j - V_w) = F_1 \quad (68)$$

For a given aircraft drag, the thrust of a propulsor located in the wake is equal to the thrust of a propulsor located in the free-stream. As such, while the ingestion of the aircraft wake reduces the net thrust of the aircraft, it does not reduce the thrust of the propulsor required. The re-energisation of the wake merely increases the propulsive efficiency of the propulsor.

C Radial Equilibrium Theory

With hub-tip ratios less than about 4/5, the radial velocities through a blade row may become appreciable. The consequent redistribution of mass flow (with respect to radius) will affect the outlet velocity profile and hence, the flow angle distribution. Given the low hub-tip ratio of less than 1/2, an analysis of *the radial equilibrium method* is conducted to determine the axial velocity distribution across the blades at the inlet and exit of the rotor.

The *radial equilibrium equation* is given by,

$$\frac{dh_0}{dr} - T \frac{ds}{dr} = V_x \frac{dV_x}{dr} + \frac{V_\theta}{r} \frac{d(r\theta)}{r} \quad (69)$$

If the change in entropy s remains approximately the same at all radii, $\frac{ds}{dr} \approx 0$, then the equation becomes:

$$\frac{dh_0}{dr} = V_x \frac{dV_x}{dr} + \frac{V_\theta}{r} \frac{d(r\theta)}{r} \quad (70)$$

If the stagnation enthalpy is assumed to be uniform and constant at the rotor inlet then the change with radius of the stagnation enthalpy across a streamline is given by:

$$h_{0,2} = h_{0,1} + \Delta h_0 \quad (71)$$

$$\frac{dh_{0,2}}{dr} = \frac{d(\Delta h_0)}{dr} \quad (72)$$

The variation of the swirl distribution in the rotor is given by:

$$V_\theta r^n = k \quad (73)$$

where k is a constant to be determined.

For a free vortex distribution, $n = 1$ and for a forced vortex distribution $n = -1$. By definition of the stage loading coefficient and assuming a uniform axial inlet velocity distribution, $V_{\theta,1} = 0$, the *Euler Equation* gives the stagnation enthalpy change across the rotor as a function of the radius:

$$\Delta h_0 = V_{\theta,2} U = \frac{k}{r^n} \quad (74)$$

Given the boundary conditions for the flow and stage loading coefficients at mid-span, the *radial equilibrium equation* can now be solved for the axial velocity distribution at the rotor exit.

$$(V_x)_m = U_m \phi_m = r_m \omega \phi_m \quad (75)$$

$$k = \omega \psi_m r_m^{n+1} \quad (76)$$

The *Forward and Backward Euler methods* [26] were used to discretise the spacial derivatives. The axial velocity at each point across the span is then iteratively solved using the following discretised *radial equilibrium equation*,

$$V_x^{n+1} = V_x^n + \frac{\Delta h_0^{n+1} - \Delta h_0^n}{V_x^n} - \frac{V_\theta^n}{V_x^n} (V_\theta^{n+1} - V_\theta^n) - \frac{(V_\theta^n)^2}{V_x^n} \frac{\Delta r}{r} \quad (77)$$

$$V_x^{n-1} = V_x^n - \frac{\Delta h_0^n - \Delta h_0^{n-1}}{V_x^n} + \frac{V_\theta^n}{V_x^n} (V_\theta^n - V_\theta^{n-1}) + \frac{(V_\theta^n)^2}{V_x^n} \frac{\Delta r}{r} \quad (78)$$

D Detailed Blade Design Parameters

Parameter	Value	Units	Parameter	Value	Units
U_m	43.9	m/s	\dot{m}	0.11	kg/s
V_∞	20	m/s	$\Delta \bar{h}_0$	748	kJ/kg
V_j	33.9	m/s	$\Delta \bar{P}_0$	449	Pa
Ω	18,000	rpm	F	1.57	N
NR	1.4		P_{motor}	86	W

Table 11: Design point parameters

Angle	Hub	Mid	Span	Angle	Hub	Mid	Span
α_1	0	0	0	δ	9.1	6.3	4.9
β_1	-48.2	-59.0	-63.0	χ_1^r	53.2	64.0	68.0
α_2	40.1	30.3	23.7	χ_2^r	20.0	52.3	61.8
β_2	-15.4	-47.3	-56.8	χ_2^s	19.8	6.6	15.6
i_1	-5	-5	-5	χ_3^s	0	0	0
i_2	-5	-5	-5				

Table 12: Flow and Blade Angles

E Power Law Boundary Layer Profile

A power law boundary layer was used to simulate the velocity profile for a turbulent flow, which is based on empirical data and was suggested by Prandtl [14].

$$\frac{V(y, z)}{V_\infty} = \left(\frac{z}{\delta(y)} \right)^n \quad (79)$$

where n is typically taken to be $1/7$.

The aircraft wake was initially simulated as a flat plate boundary layer profile as shown in Fig. 3. The drag and shape factor of the simulated boundary layers were calculated for the range of boundary layer profiles shown in Fig. 33. The shape factor, H , displacement thickness, δ^* , and momentum thickness, θ , are defined as follows:

$$H = \frac{\delta^*}{\theta} \quad (80)$$

$$\delta^*(y) = \int_0^\infty \left(1 - \frac{V(y, z)}{V_\infty} \right) dz \quad (81)$$

$$\theta(y) = \int_0^\infty \frac{V(y, z)}{V_\infty} \left(1 - \frac{V(y, z)}{V_\infty} \right) dz \quad (82)$$

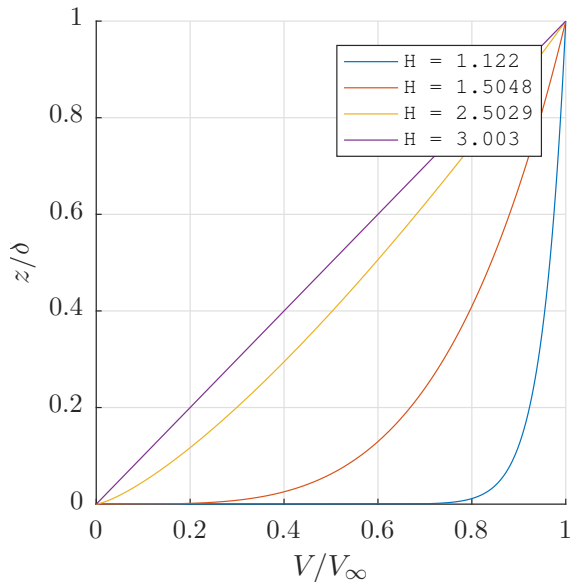


Figure 33: Boundary Layer Velocity Profiles

The drag on the plate due to the momentum deficit in the wake is given by the following momentum integral:

$$D = \rho \int_S (V_\infty - V(y, z)) V(y, z) dS \quad (83)$$

F Transformation from Cartesian to Polar

The radial and tangential components of the velocity are given by:

$$V_r = \pm \frac{V_x}{\cos(\alpha)} \cos(\theta)$$

$$V_\theta = \pm \frac{V_x}{\cos(\alpha)} \sin(\theta)$$

where:

$$\alpha = \tan^{-1} \left(\frac{y}{x} \right)$$

$$\beta = \tan^{-1} \left(\frac{V_y}{V_x} \right)$$

$$\theta = \alpha - \beta$$

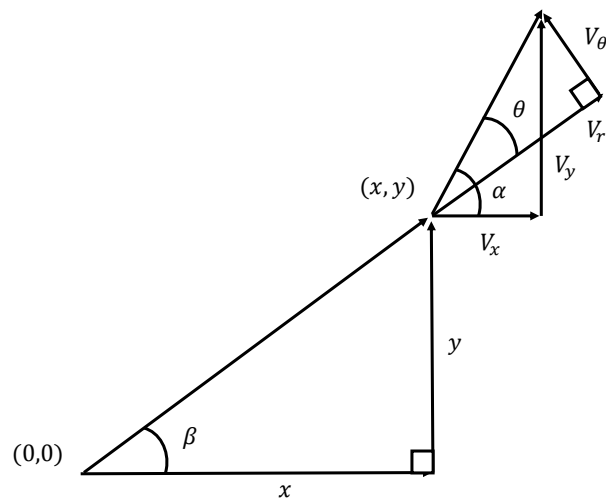


Figure 34: Cartesian to Polar Transformation

G Blade Design Theory

Radial Equilibrium Theory

With hub-tip ratios less than about 4/5, the radial velocities through a blade row may become appreciable. The consequent redistribution of mass flow (with respect to radius) will affect the outlet velocity profile and hence, the flow angle distribution.

Given the low hub-tip ratio of less than 1/2, an analysis of *the radial equilibrium method* is conducted to determine the axial velocity distribution across the blades at the inlet and exit of the rotor.

The *radial equilibrium equation* is given by,

$$\frac{dh_0}{dr} - T \frac{ds}{dr} = V_x \frac{dV_x}{dr} + \frac{V_\theta}{r} \frac{d(r\theta)}{r}$$

It can be shown that the axial velocity at each point across the span can be iteratively solved using the following discretized *radial equilibrium equation*

The variation of the stage loading with radius for a forced and free vortex distribution are given by,

$$V_\theta r^n = k_1$$

For a free vortex distribution, $n = 1$ and for a forced vortex distribution $n = -1$. Using the Euler Equation the stage loading distribution can then be determined.

$$\psi = \frac{\Delta h_0}{U^2} = \frac{V_\theta}{\omega r} = \frac{k_1}{\omega r^{n+1}}$$

Given at $r = r_m$, $\psi = \psi_m$

$$\begin{aligned} k_1 &= \omega \psi_m r_m^{n+1} \\ \therefore \psi &= \psi_m \left(\frac{r_m}{r} \right)^{n+1} \end{aligned}$$

Propulsor Control Volume Analysis

$$U = r_m \omega$$

$$V_x = U \phi$$

$$\dot{m} = \rho V_x A_2$$

$$A_2 = \pi(r_c^2 - r_h^2)$$

Assuming no stagnation pressure loss from the free stream to the propulsor inlet,

$$p_{01} = p_\infty + \frac{1}{2} \rho V_\infty^2$$

Assuming no stagnation pressure loss through the inlet to the rotor,

$$p_{02} = p_{01}$$

The mass-averaged stagnation enthalpy and stagnation pressure change across a stream-line for the rotor stage are given by

$$\Delta h_0 = \psi U^2$$

$$\Delta H_0 = \oint h_0 d\dot{m}$$

$$\overline{\Delta h_0} = \frac{\Delta H_0}{\dot{m}}$$

$$\overline{\Delta p_0} = \rho \overline{\Delta h_0} \eta_{is}$$

It is assumed that due to mixing of the flow, downstream of the rotor the stagnation quantities will be approximately uniform across the radius. As such, the absolute values are used in all further calculations. The reduction in stagnation pressure due to the mixing is assumed to be negligible.

$$p_{03} = p_{02} + \overline{\Delta p_0}$$

Assuming negligible stagnation pressure loss across the stator or nozzle,

$$p_{05} = p_{03}$$

The flow at the exit of the nozzle is subsonic and hence the exit pressure is approximately atmospheric, $P_5 = P_\infty$. Hence, assuming constant density ($M < 0.3$) and applying mass continuity and Bernoulli across the sections, the nozzle ratio can be derived.

$$V_5 = \sqrt{\frac{2}{\rho}(p_{05} - p_\infty)}$$

Assuming the swirl at the exit from the stator is negligible such that $V_4 \approx V_{4x} = V_x$. The nozzle ratio is thus given by:

$$NR = \frac{A_4}{A_5} = \frac{V_5}{V_4}$$

The thrust and power were calculated by applying a control volume around the propulsor such that the pressure is at ambient conditions.

$$F = \dot{m}(V_j - V_\infty)$$

$$P = \frac{\dot{m} \Delta h_0}{\eta_{motor}}$$

$$P_{KE} = \frac{1}{2} \dot{m} (V_j^2 - V_\infty^2)$$

Flow Angles

Assuming axial inlet flow, the relative and absolute flow angles at a given radius, r , are given by,

$$\begin{aligned}\alpha_1 &= 0^\circ \\ \beta_1 &= -\arctan\left(\frac{1}{\phi(r)}\right) \\ \alpha_2 &= \arctan\left(\frac{\psi(r)}{\phi(r)}\right) \\ \beta_2 &= -\arctan\left(\frac{1}{\phi(r)} - \tan(\alpha_2)\right)\end{aligned}$$

Blade Number and Chord Length

The pitch-chord ratio was derived using Lieblein's equation and a diffusion factor of $DF = 0.45$.

$$\begin{aligned}DF &= 1 - \frac{W_2}{W_1} + \frac{1}{2} \frac{\Delta V_\theta}{W_1} \frac{l}{c} \\ DF &= 1 - \frac{\cos(\beta_1)}{\cos(\beta_2)} + \frac{1}{2} \cos(\beta_1) |\tan(\beta_2) - \tan(\beta_1)| \frac{l}{c}\end{aligned}$$

The mid-span chord length is calculated from the rotor and stator blade aspect ratios.

$$s = r_c - r_h$$

$$c_m = \frac{s}{AR}$$

$$l_m = \left(\frac{l}{c}\right)_m c_m$$

The mean-line circumference was used to determine the number of rotor and stator blades.

$$Z_b \geq \frac{2\pi r_m}{l}$$

The pitch-chord ratio variation across the span was calculated using Lieblein and a constant DF condition. This leads to low pitch-chord ratios at the hub and high pitch-chord ratios at the tip. The pitch at a given radius is then given by,

$$l = \frac{2\pi r}{Z_b}$$

The chord lengths for the rotor and stator across the span can then be determined by,

$$c = \frac{l}{\left(\frac{l}{c}\right)}$$

Metal Angles

The divergence of the flow from the metal angle of the blade is known as deviation, and is a result of both viscous and inviscid effects. The inviscid component is due to the diffusion of the flow as it diverges at the trailing edge of the blade, whilst the viscous effect is due to boundary layer growth and flow separation that may occur on the suction surface of the blade. From (insert Figure), it can be seen that as the deviation of the blade increases, the stage loading decreases. This effect becomes even more significant at higher flow coefficients.

Blade camber and stagger are defined as,

$$\theta = \chi_1 - \chi_2 = \beta_1 - \beta_2$$

$$\gamma = \frac{\chi_1 + \chi_2}{2}$$

Deviation,

$$\delta = \beta_2 - \chi_2$$

$$\delta \approx m\theta \sqrt{\frac{l}{c}} \quad (84)$$

where m is given by the formula,

$$m = 0.23 \left(\frac{2a}{c} \right)^2 + 0.1 \left(\frac{\chi_2}{50} \right)$$

For circular arc camber line, $\frac{2a}{c} = 1$.

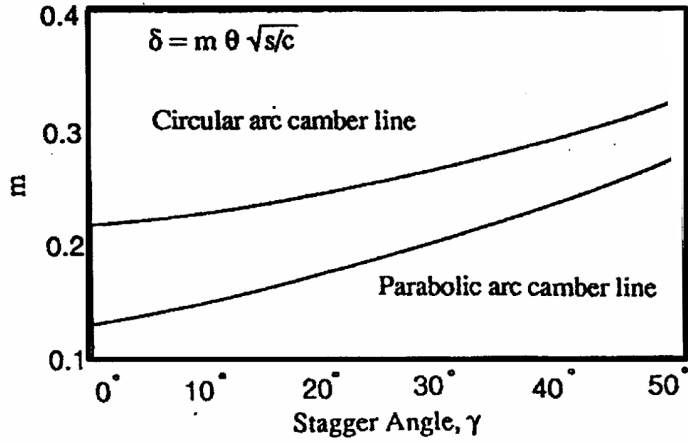


Figure 35: Variation of the parameter m parameter for determining deviation

Carter's rule (Eqn. 84) is an empirical correlation for predicting the blade deviation at high Re . However, given the low Re of the compressor for this project, the deviation predicted is likely to be inaccurate as research on low Re has shown that Carter's rule underestimates the deviation [12].

The metal angles for the blades are defined as:

$$\chi_1^r = \beta_1 - i_1$$

$$\chi_2^r = \chi_1^r - \theta$$

$$\beta_2 = \chi_2^r + \delta$$

The metal angles of the stator are recalculated to compensate for the change in flow angles due to the deviation and incidence of the rotor stage.

$$W_2 = \cos(\beta_2)$$

$$W_{\theta 2} = \sin(\beta_2)$$

$$V_{\theta 2} = U + W_{\theta 2} = r\omega + W_{\theta 2}$$

$$\alpha_2 = \arctan \left(\frac{V_{\theta 2}}{V_x} \right)$$

The metal angles for the stator are given by,

$$\chi_2^s = \alpha_2 - i_2$$

$$\chi_3^s = 0$$

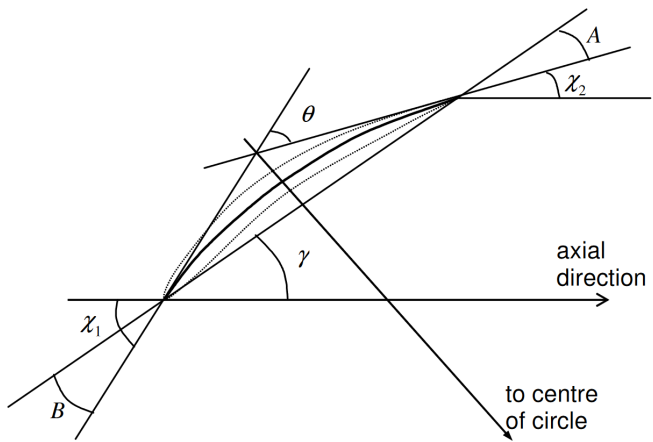


Figure 36: Geometry of a circular arc camber line compressor blade [23]

H Traverse Control Volume Analysis

Mass flow rate:

$$\dot{m} = \sum_i \sum_j (V_x)_{ij} \rho_{ij} \Delta y \Delta z \quad (85)$$

Steady-Flow Momentum Equation:

$$F = \sum_i \sum_j (V_x)_{ij}^2 \rho_{ij} \Delta y \Delta z + \sum_i \sum_j p_{ij} \Delta y \Delta z \quad (86)$$

Steady-Flow Energy Equation (adiabatic flow):

$$-\dot{W}_x = \dot{m} \Delta h_0 \quad (87)$$

$$-\dot{W}_x = \dot{m} c_p \Delta T_0 \quad (88)$$

$$-\dot{W}_x = \dot{m} (c_p \Delta T + V^2 / 2) \quad (89)$$

where $T = p/\rho R$ from the ideal gas equation.

Steady-Flow Energy Equation alternative definition:

$$-\dot{W}_x = \dot{m} \Delta h_0 \quad (90)$$

$$-\dot{W}_x = \frac{\dot{m} \Delta p_0}{\rho} + T_0 \Delta s \quad (91)$$

$$-\dot{W}_x = \dot{m} (\Delta p / \rho + V^2 / 2) + T_0 \Delta s \quad (92)$$

$$P_{Shaft} = P_{Mech} + P_{Lost} \quad (93)$$

where P_{Mech} is the mechanical energy of the flow and P_{Lost} is the irreversible energy loss.

Kinetic and Mechanical Energy:

$$P_{KE} = \sum_i \sum_j V_{ij}^2 (V_x)_{ij} \rho_{ij} \Delta y \Delta z \quad (94)$$

$$P_{Mech} = \sum_i \sum_j (p_0)_{ij} (V_x)_{ij} \Delta y \Delta z \quad (95)$$

$$P_{Shaft} = \sum_i \sum_j c_p \Delta T_{ij} (V_x)_{ij} \Delta y \Delta z + P_{KE} \quad (96)$$

Due to the loss of significance error as a result of subtracting two large numbers that approximately cancel, the percentage error in the first term of the RHS of eq. 96 is very large. As such, it is approximated that the inlet and outlet temperatures are approximately equal such that:

$$P_{Shaft} \approx P_{KE} \quad (97)$$

The propulsor isentropic efficiency is defined as:

$$\eta = \frac{P_{Mech}}{P_{Shaft}} \quad (98)$$

5 References

- [1] Plas, A. P., Sargeant, M. A., Madani, V., Crichton, D., Greitzer, E. M., Hynes, T. P., and Hall, C. A., "Performance of a Boundary Layer Ingestion (BLI) Propulsion System", *AIAA Paper 2007-450*, 2007.
- [2] Sequeira, C., *Hybrid Air Vehicles*, personal communication during visit to Cardington Bedford, Bedford, 2017.
- [3] Carichner, G., and Nicolair, L., "Hybrids...the Airship Messiah?", *AIAA Paper 2013-1317*, March 2013.
- [4] "Airlander 10 Technical Details", <https://www.hybridairvehicles.com>, 2017.
- [5] Carrión, M., Steijl, R., and Barakos, G. N., "Analysis of Hybrid Air Vehicles Using Computational Fluid Dynamics", *AIAA Journal*, Vol. 53, No. 4, July-August 2016.
- [6] Drela, M., "Power Balance in Aerodynamic Flows", *AIAA Paper 2009-3762*, 2009.
- [7] Li, J. "Cambridge University Engineering Department 3A1 Lecture Notes", 2015.
- [8] Smith, L. H., "Wake Ingestion Propulsion Benefit", *Journal of Propulsion of Power*, Vol. 9, No1. 1, pp. 74-82, 1993.
- [9] Jacobs, E. N., Ward, K. E., and Pinkerton, R. M., "The Characteristics of 78 Related Airfoil Sections from Tests in the Variable-density Wind Tunnel", *NACA Rept.*, No. 460, 1932.
- [10] Barlow, J. B., William, H., and Pope, A., "Low-Speed Wind Tunnel Testing", *John Wiley and Sons*, 1999.
- [11] Hoerner, S. F., "Fluid Dynamic Drag: Practical Information on Aerodynamic Drag and Hydrodynamic Resistance", *Midland Park, NJ, Chap. 6*, 1958.
- [12] Maffiolo, A., Hall, C., and Melvin, S., "Aerodynamics of low reynolds number axial compressor sections", *53rd AIAA Aerospace Sciences Meeting*, Jan 2015.
- [13] Uranga, A., Drela, M., Greitzer, E. M., et al., "Preliminary Experimental Assessment of the Boundary Layer Ingestion Benefit for the D8 Aircraft", *AIAA Paper 2014-0906*, 2014.
- [14] Prandtl, L., "The mechanics of viscous fluids", in *Aerodynamic Theory III*, W.F. Durand (Ed.), vol. 3, pp. 34-208, Julius Springer, Berlin, 1995.
- [15] To, H. and Miller, R. J., "The Effect of Aspect Ratio on Compressor Performance", *ASME. Turbo Expo: Power for Land, Sea, and Air, Volume 2A: Turbomachinery*, 2015.
- [16] Atinault, O., Carrier, G., Grenon, R., Verbecke, C., and Viscaat, P., "Numerical and Experimental Aerodynamic Investigations of Boundary Layer Ingestion for Improving Propulsion Efficiency of Future Air Transport", *AIAA Paper 2013-2406*, 2013.
- [17] Carter, A. D. S., and Hughes, Hazel P., "A Theoretical Investigation into the Effect of Profile Shape on the Performance of Airfoils in Cascade", *R. & M. No. 2384, British A. R. C.*, 1946.

- [18] Cumpsty, N.A. and Horlock, J.H., “Averaging non-uniform flow for a purpose”, *ASME -Journal of Turbomachinery*, January 2006, Vol. 128, pp. 120-129, 2006.
- [19] Grimshaw, S., *MHI Turbomachinery Research Fellow at Girton College*, personal communication, 2017.
- [20] Pantelidis, K., *Research student, University of Cambridge*, personal communication, 2017.
- [21] Drela M., “XFOIL: An Analysis and Design System for Low Reynolds Number Airfoils”, *Mueller T.J. (eds) Low Reynolds Number Aerodynamics. Lecture Notes in Engineering, vol 54. Springer, Berlin, Heidelberg*, 1989.
- [22] Dixon, S., and Hall, C., “Fluid Mechanics and Thermodynamics of Turbomachinery”, *Butterworth-Heinemann*, 2013.
- [23] Atkins, N., and Hynes, T. “Cambridge University Engineering Department 4A3 Lecture Notes”, 2017.
- [24] Buerge, B. T., “The Suitability of Hybrid vs. Conventional Airships for Persistent Surveillance Missions”, *AIAA Paper 2010-1014*, 2010.
- [25] Sabo, K., and Drela, M., “Benefits of Boundary Layer Ingestion Propulsion”, *AIAA Paper 2015-1667*, 2015.
- [26] Press, W. H., Flannery, B. P., Teukolsky, S. A., and Vetterling, W. T, “Numerical Recipes in FORTRAN: The Art of Scientific Computing”, *2nd ed. Cambridge, England, Cambridge University Press, p. 710*, 1992.